


## Article

# Numerical Simulation of Hydrate Dissociation Behaviors in Hydrate Reservoir with Different Properties during Horizontal Well Drilling

Fei Gao <sup>1,2,3</sup>, Yu Zhang <sup>1,2,3,\*</sup>, Chang Chen <sup>1,2,3</sup>, Xiaosen Li <sup>1,2,3,\*</sup> and Zhaoyang Chen <sup>1,2,3</sup> 

- <sup>1</sup> School of Energy Science and Engineering, University of Science and Technology of China, Hefei 230026, China; gaofei@ustc.edu.cn (F.G.); chenchang@ms.giec.ac.cn (C.C.); chenzy@ms.giec.ac.cn (Z.C.)
- <sup>2</sup> Key Laboratory of Gas Hydrate, Guangzhou Institute of Energy Conversion, Chinese Academy of Sciences, Guangzhou 510640, China
- <sup>3</sup> Guangdong Provincial Key Laboratory of New and Renewable Energy Research and Development, Chinese Academy of Sciences, Guangzhou 510640, China
- \* Correspondence: zhangyu1@ms.giec.ac.cn (Y.Z.); lixs@ms.giec.ac.cn (X.L.); Tel.: +86-20-8705-8054 (Y.Z.); +86-20-8705-7037 (X.L.)

**Abstract:** The effectiveness of horizontal well drilling in improving the gas recovery efficiency of hydrate production makes it a promising technology for commercial exploitation. However, during horizontal well drilling in hydrate reservoirs, it is crucial to control hydrate dissociation to ensure the reservoir stability and drilling safety. In this work, a two-dimensional model using polar coordinates was built to study the influences of hydrate reservoir characteristics and drilling fluid salinity on gas production. The simulation applies to the hydrate reservoir of the second natural gas hydrate (NGH) production test in the Shenhu area of the South China Sea. The characteristics of hydrate dissociation and secondary formation and the drilling invasion behavior in the NGH layer and the mixing layer (free gas + hydrate) during horizontal well drilling were analyzed and compared. The simulation results indicated that the pressure and temperature transmission rates in the mixing layer (free gas + hydrate) are higher than those in the NGH layer. The invasion amount of drilling fluid in the mixing layer is 18.8 times more than that in the NGH layer. Under the high invasion of the drilling fluid, the hydrate dissociation amount in the mixing layer is similar to that of the NGH layer even though the initial hydrate saturation of the NGH layer was 2.65 times that of the mixing layer. The area of the hydrate dissociation in the mixing layer is much larger than that in the NGH layer, which may lead to the increase in risk of wellbore instability. The secondary hydrate formation is only observed in the NGH layer, which inhibits the drilling fluid invasion. The salinity of the drilling fluid has a more significant impact on the hydrate dissociation near the wellbore in the mixing layer compared to the NGH layer. With the increase in salinity from 3.05 wt% to 20 wt%, the hydrate dissociation range in the mixing layer increases from 0.16 m to 0.23 m, while the hydrate dissociation range in the NGH layer does not significantly change.

**Keywords:** natural gas hydrate; horizontal well; drilling process; reservoir property; hydrate dissociation



**Citation:** Gao, F.; Zhang, Y.; Chen, C.; Li, X.; Chen, Z. Numerical Simulation of Hydrate Dissociation Behaviors in Hydrate Reservoir with Different Properties during Horizontal Well Drilling. *J. Mar. Sci. Eng.* **2024**, *12*, 554. <https://doi.org/10.3390/jmse12040554>

Academic Editor: Dmitry A. Ruban

Received: 26 February 2024

Revised: 22 March 2024

Accepted: 22 March 2024

Published: 26 March 2024



**Copyright:** © 2024 by the authors. Licensee MDPI, Basel, Switzerland. This article is an open access article distributed under the terms and conditions of the Creative Commons Attribution (CC BY) license (<https://creativecommons.org/licenses/by/4.0/>).

## 1. Introduction

Natural gas hydrate (NGH) is widely distributed in permafrost and marine sediments. It has been considered as a potential unconventional energy source in the future due to its vast reserves and high energy density [1]. To exploit NGH resources, scholars have proposed various production methods, such as depressurization [2,3], thermal stimulation [4,5], chemical injection [6,7], and CO<sub>2</sub> replacement [8]. Depressurization is the reduction of pressure around wellbore by pumping water or gas from the formation, which is widely used. Thermal stimulation raises the temperature of the NGH region above the phase-equilibrium temperature. The hydrate phase equilibrium is also affected by thermodynamic inhibitors, so chemicals can be injected to exploit NGH. The main consequence of

CO<sub>2</sub> replacement is to drastically reduce the dissociation of hydrate structures, which is to ensure the stability of the reservoir. Several countries have carried out field exploration tests to exploit NGH [9–14]. In 2017 and 2020, China carried out hydrate exploration with depressurization in the Shenhu area of the South China Sea, using both vertical wells and horizontal wells, demonstrating the feasibility of NGH exploitation in clayey silt reservoirs [13]. The results of the production test showed that horizontal wells can achieve an average daily gas production 5.57 times higher than that of vertical wells [14].

Horizontal wells can effectively accelerate the propagation speed of temperature and pressure, extend the contact length between the wellbore and the hydrate reservoir, and accelerate the production of gas and water, thus realizing pressure reduction more quickly and improving the speed of hydrate exploration [15–19]. Therefore, horizontal well drilling technology is considered highly promising for the commercial exploitation of NGH [14]. The research also showed that hydrate exploration using horizontal wells has challenges such as high water production, difficult drilling, reservoir subsidence, and obvious geological settlement affecting the pressure drop rate, and wellbore stability issues have been discovered [20–23]. The drilling process is essential in ensuring the safe and sustainable exploitation of hydrates. The NGH reservoirs have unique geological conditions, shallow buried depth, poor stability, and a complex and difficult drilling environment [24]. Therefore, it is extremely important to guarantee the stability of the reservoir during the drilling process [25]. In the process of horizontal drilling, the drilling length is larger and multiple reservoirs with different characteristics are experienced. The research on physical properties changes around the wellbore and the patterns of hydrate dissociation during horizontal well drilling in NGH reservoirs with varying geological parameters is crucial for achieving safe and controlled exploitation.

In the early stages, extensive research has been conducted on the drilling process of hydrate reservoirs, mainly through numerical simulation. Freij-Ayoub et al. [26] established a coupled numerical model for evaluating wellbore stability in hydrate sediments. The results showed that higher drilling fluid temperature could increase pore pressure, leading to hydrate dissociation and ultimately reducing the stability of hydrate reservoirs. Khabibullin et al. [27] further found that the main parameters influencing hydrate dissociation are drilling fluid temperature and bottom hole pressure. The increase in drilling fluid temperature or the decrease in bottom hole pressure could promote hydrate dissociation. Ning et al. [28,29] used Tough + Hydrate to study the effects of drilling mud properties (the density, temperature, and salinity) and the effects of geophysical properties of sediments on the drilling fluid invasion and hydrate stability. They found that the low saturation and high permeability of the hydrate reservoir are vulnerable to fluid invasion, and high hydrate saturation zones appear during the process of drilling fluid invasion. Sun et al. [30] analyzed the wellbore stability problems during the drilling process by numerical simulation. The results showed that the increase in drilling fluid temperature and salinity will promote hydrate dissociation, resulting in more free gas near the wellbore and an increase in local pore pressure. Yu et al. [31] built a two-dimensional numerical model to analyze the behaviors of hydrate dissociation during drilling in hydrate reservoirs, and found that gas flows into the wellbore during the drilling process. Gao et al. [32] investigated the heat transfer in hydrate-bearing reservoirs during drilling fluid invasion through experimental simulation, and found that the higher the reservoir's initial temperature, the earlier the hydrate reservoir reaches phase equilibrium and the faster the hydrate decomposes. Huang et al. [33] carried out experiments to study the drilling process in hydrate-bearing sediments with different rates of drilling fluid circulation. The results showed that a faster drilling fluid circulation rate could lead to a faster hydrate dissociation rate, which is detrimental to wellbore stability. Wei et al. [34] established a wellbore-formation coupled model to analyze the induced mechanisms of bottomhole pressure drops, wellbore blockages, and methane emission. The simulation results show that the increase in free gas increases the possibility of well collapse, hydrate dissociation, and gas intrusion, while low flow rates can lead to free gas intrusion and wellbore plugging. Huang et al. [35] and Zhang et al. [36]

respectively established one-dimensional and two-dimensional numerical models of the drilling fluid invasion process and studied the influences of drilling temperature and salinity as well as permeability on the reservoirs. They found that high-intrinsic permeability extends the ranges of drilling fluid invasion and hydrate dissociation, and that the higher temperature of drilling fluid promotes the dissociation of hydrate in the reservoir around the wellbore, with secondary hydrate formation. Li et al. [37] investigated the effects of drilling fluid density on both the hydrate dissociation and borehole collapse by building a coupled model. The results showed that the influence of the drilling fluid invasion process on the reservoir pressure is much greater than that of temperature. Moreover, the increase in drilling fluid density could inhibit the hydrate dissociation near the wellbore. Zhao et al. [38] conducted experiments and numerical simulations to study the temperature distribution of vertical drilling wells in hydrate layers of the South China Sea. The results revealed that the well permeability has the most significant impact on well temperature, while the hydrate saturation has little influence on the well temperature. Li et al. [39] developed a wellbore stability analysis model, indicating that maintaining drilling fluid temperature below the formation temperature effectively inhibits hydrate dissociation in the wellbore area. When the wellbore temperature increases or the pressure decreases, the dissociation rate of the hydrate near the wellbore accelerates, and the wellbore instability area will further expand.

In the process of drilling horizontal wells, due to the longer drilling lengths, the geological conditions become more complex and variable. Several studies have focused on the drilling safety and wellbore stability of horizontal drilling in hydrate reservoirs. Wang et al. [40] investigated the impact of drilling fluid invasion on hydrate dissociation behavior using numerical simulation with varied drilling fluid parameters in a horizontal well. They found that the drilling fluid temperature has a great influence on hydrate reservoirs. The increase in salinity accelerates the dissociation of hydrate. Li et al. [41] established a model to calculate the mud weight window (MWW) for horizontal wells drilled into hydrate reservoirs, and found that hydrate saturation significantly affects collapse pressure, but has a small effect on the fracture pressure. Sun et al. [42] studied the wellbore stability in the process of horizontal well drilling through numerical simulation. The results showed that the significant increase in the drilling fluid temperature can greatly affect the wellbore stability, and even lead to the formation of secondary hydrate and blowout. With the decrease in initial hydrate saturation and irreducible water saturation, the wellbore instability intensifies, and the low permeability mud cake helps to reduce fluid loss, thereby enhancing the wellbore stability. Liao et al. [43] established a fully coupled wellbore-reservoir model for horizontal well drilling in hydrate reservoirs. They found that the drilling fluid inlet temperature plays an absolute dominant role in the wellbore extension length. In the process of drilling, the hydrate dissociation and wellbore stability are also affected by reservoir properties such as permeability, hydrate saturation, porosity, and gas pressure.

In summary, controlling drilling parameters and fluid properties is crucial for managing hydrate dissociation near the wellbore, ensuring wellbore stability and maintaining drilling safety. Currently, extensive research has been conducted on drilling parameters and fluid properties, with most studies focusing on the vertical well drilling process, with limited research on horizontal drilling processes, especially under different reservoir characteristics. Therefore, this study aims to address this gap by establishing a two-dimensional polar coordinate numerical model of horizontal well drilling in the hydrate reservoirs. In view of the second production test in the Shenhua area of the South China Sea, based on the relevant geological conditions and parameters, the two-dimensional response characteristics of the temperature, pressure, salinity, and gas–liquid–solid three-phase saturations of the hydrate reservoir in horizontal well drilling were simulated. The hydrate dissociation behaviors and physical property changes of the reservoir during horizontal well drilling in different reservoir layers were investigated. Additionally, the influence of the salinity of the drilling fluid on the hydrate dissociation in the reservoir was studied.

## 2. Geological Setting

The second production test area of China is located in the Baiyun Sag of the Pearl River Mouth Basin in the northern Shenhu Sea area of the South China Sea, as shown in the red frame of Figure 1. This area has rich NGH resources, with a relatively thick hydrate reservoir and high hydrate saturation [14]. The hydrate deposit is located at a depth of 207–297 m below the seabed, with a water depth of 1225 m. The hydrate is mainly deposited in the unconsolidated clayey silt within Quaternary. The hydrate reservoir contains three layers: (1) an NGH layer; this layer consists of solid hydrate and liquid water, with an average effective porosity of 0.373, average hydrate saturation of 0.31, and average permeability of 2.38 mD; (2) a mixing layer, comprising solid hydrate, liquid water, and gaseous hydrocarbon; this layer has an average effective porosity of 0.346, average hydrate saturation of 0.117, and average permeability of 6.63 mD; (3) a gaseous hydrocarbon layer; this layer contains liquid water and gaseous hydrocarbon, with an average effective porosity of 0.347, average gas saturation of 0.073, and average permeability of 6.8 mD. The geological and physical parameters of each layer in the hydrate reservoir are summarized in Table 1. Horizontal well technology has been implemented in this hydrate production test, and the wellbore structure data can be observed in Figure 2. In this study, only the horizontal section is utilized to establish the numerical simulation model, while a detailed explanation of the physical model and grid processing will be subsequently provided.

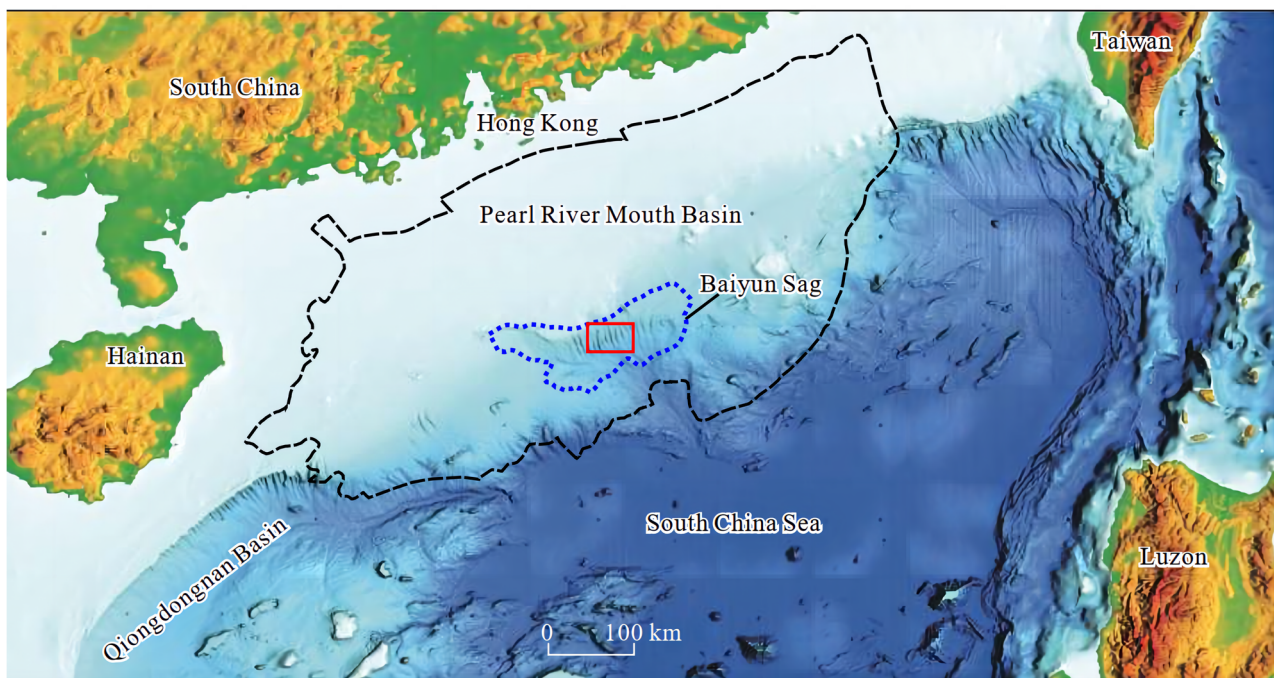


**Figure 1.** Geological background and location of the second NGH production test of China [14].

**Table 1.** Geological and physical parameters of hydrate reservoirs in each layer in the second NGH production test in the Shenhu Sea area [14].

Layer	Depth (m bsf)	Thickness (m)	Effective Porosity (%)	Permeability (mD)	Saturation		
					$S_h$ (%)	$S_g$ (%)	$S_w$ (%)
NGH layer	207.8~253.4	45.6	37.3	2.38	0.31	0	0.69
Mixing layer	253.4~278	24.4	34.6	6.63	0.117	0.132	0.751
Free gas layer	278~297	19	34.7	6.8	0	0.073	0.927



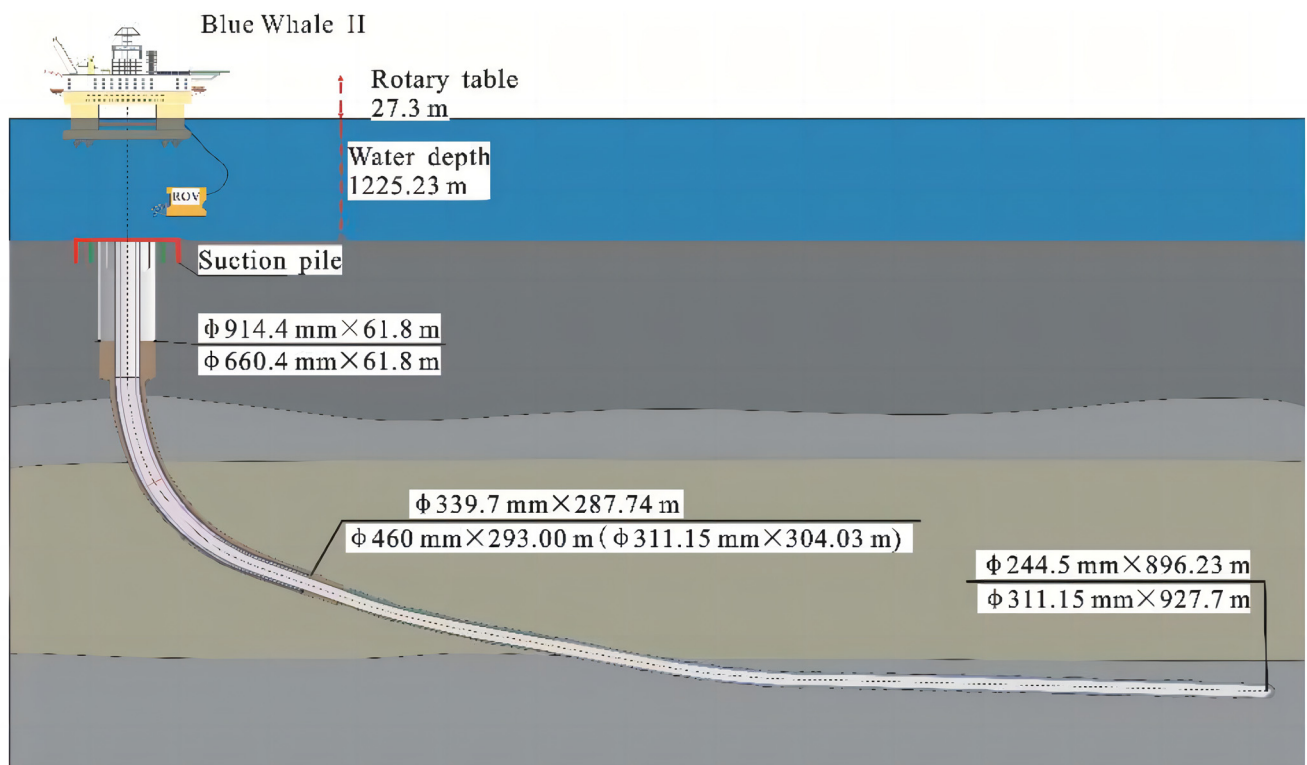


**Figure 2.** Wellbore structure of horizontal well in the second NGH production test of China [14].

The geological parameters of the hydrate reservoir were not fully disclosed by the test-production site. Therefore, for the simulation calculation, other relevant physical parameters were adopted from the physical parameters of hydrate-bearing sediments at the W17 station of the South China Sea [36], as presented in Table 2 below.

**Table 2.** Physical parameters of hydrate reservoir at W17 station.

Parameter	Value	Parameter	Value
Formation temperature gradient	0.0443 K/m	Kinetic viscosity of methane/ $\mu_g$	$2.45 \times 10^{-12}$ MPa·s
Initial seawater mass density/ $\rho_w$	1019 kg/m <sup>3</sup>	Mass density of hydrate/ $\rho_h$	920 kg/m <sup>3</sup>
Pore gas saturation of layer/ $\rho_r$	2600 kg/m <sup>3</sup>	Pore water salinity/ $X_{sc}$	3.05 wt%
Wellbore radius/ $r_w$	0.1 m	Thermal conductivity of methane gas/ $\lambda_g$	0.07 W/m·K
Initial temperature of hydrate reservoir/ $T_0$	14.82 °C	Thermal conductivity of hydrate/ $\lambda_h$	0.6 W/m·K
Initial pressure of hydrate reservoir/ $P_0$	14.908 MPa	Geotechnical thermal conductivity of frame/ $\lambda_r$	2.5 W/m·K
Hydrate specific heat capacity/ $C_h$	2.1 kJ/kg·K	Drilling fluid temperature/ $T_f$	16.0 °C
Geotechnical specific heat capacity of frame/ $C_r$	0.71 kJ/kg·K	Drilling fluid pressure/ $P_f$	15.34 MPa
Methane specific heat capacity/ $C_g$	2.2 kJ/kg·K	Enthalpy of hydrate dissociation/ $\Delta H$	54.2 kJ/mol
Salt diffusion coefficient/ $K_{DD}$	$1.76 \times 10^{-9}$ m <sup>2</sup> /s		

### 3. Methods and Numerical Models

In this work, a numerical model of horizontal wells drilled in NGH sediments was developed. The model was established in a two-dimensional polar coordinate system and incorporated processes such as heat and mass transfer within the hydrate reservoir, kinetics of hydrate formation and dissociation, and gas–liquid two-phase seepage. Furthermore, the model considered the effects of a reservoir temperature gradient, pressure gradient, and

gravity on seepage. The model was solved using the finite difference method. To simplify the model and facilitate its solution, the following hypotheses were proposed:

- (1) All hydrates in the hydrate reservoir are assumed to be type I methane hydrate, and the hydration number is 6.0 [44].
- (2) Only gas-liquid two-phase flow is considered within the hydrate reservoir. Solid hydrates and the rock-soil frame of the reservoir are assumed to be immobile, and Darcy's law is assumed to be effectively applicable to fluids.
- (3) Both the rock-soil frame and hydrate are assumed to be incompressible.
- (4) Since the test-production site only disclosed average porosity and average hydrate, gas, and water saturation of the hydrate reservoir in Table 1, the actual distribution is not clear. The porosity of the hydrate reservoir is assumed to be constant and uniformly distributed, and the hydrate, gas, and liquid phases in the reservoir are assumed to be uniformly distributed.
- (5) Local thermal equilibrium between the sediment and the fluid in the hydrate reservoir is assumed to be maintained. A throttling effect and radiation heat transfer in the flow process are neglected.
- (6) The dissociation of hydrates in the reservoir is assumed to be a successive water–gas source with various intensity.
- (7) Changes in the physical properties of the drilling fluid are not considered, and only constant pressure, temperature, and salinity are considered.
- (8) Convective heat transfer and heat conduction in hydrate reservoirs are considered, and the influence of pore water salinity on physical parameters such as thermal conductivity is considered, while the contact thermal resistance of the fluid and the reservoir and the heat-release process of salt dissolution are neglected.
- (9) Changes in drilling length over time during horizontal drilling are neglected.

### 3.1. Mass Transfer and Gas–Liquid Two-Phase Flow Model in Hydrate Reservoir

Based on the above assumptions, the gas–liquid two-phase flow process in hydrate reservoirs is mainly the displacement of primary fluid by the drilling fluid. A two-phase flow model based on Darcy's law is adopted to describe the flow of methane and water in the porous media of hydrate reservoirs. The mass balance equations of gas, water, salinity, and hydrate are as follows:

$$\frac{\partial(\varphi\rho_g S_g)}{\partial t} = -\frac{1}{r} \frac{\partial}{\partial r}(r\rho_g v_{gr}) - \frac{1}{r} \frac{\partial}{\partial \theta}(\rho_g v_{g\theta}) + \dot{m}_g M_g \quad (1)$$

$$\frac{\partial(\varphi\rho_w S_w)}{\partial t} = -\frac{1}{r} \frac{\partial}{\partial r}(r\rho_w v_{wr}) - \frac{1}{r} \frac{\partial}{\partial \theta}(\rho_w v_{w\theta}) + \dot{m}_w M_w \quad (2)$$

$$\frac{\partial(\varphi\rho_w S_w X_s)}{\partial t} = -\frac{1}{r} \frac{\partial}{\partial r}(r\rho_w X_s v_{wr}) - \frac{1}{r} \frac{\partial}{\partial \theta}(\rho_w X_s v_{w\theta}) + k_D \left\{ \frac{1}{r} \frac{\partial}{\partial r} \left( \varphi r \rho_w S_w \frac{\partial X_s}{\partial r} \right) + \frac{1}{r} \frac{\partial}{\partial \theta} \left( \varphi \rho_w S_w \frac{\partial X_s}{\partial \theta} \right) \right\} \quad (3)$$

$$\varphi\rho_h \frac{\partial(S_h)}{\partial t} = -\dot{m}_h (M_g + n_w M_w) \quad (4)$$

where  $r$  is the radius, m;  $\theta$  is the circumferential angle, rad;  $S_g$ ,  $S_w$ , and  $S_h$  are the saturations of gas, water, and hydrate of the hydrate sediment, respectively;  $\varphi$  is the pore porosity;  $\rho_g$ ,  $\rho_w$ , and  $\rho_h$  are the densities of gas, water, and hydrate of the hydrate sediment, kg/m<sup>3</sup>;  $\dot{m}_g$ ,  $\dot{m}_w$  and  $\dot{m}_h$  are the molar sources of gas, water and hydrate, respectively, mol/m<sup>3</sup>·s;  $X_s$  is the salinity;  $M_g$  and  $M_w$  are the molar densities of methane and water, kg/mol;  $n_w$  is the hydrate number;  $v_{gr}$  and  $v_{wr}$  are the flow velocity of gas and water, respectively, in the  $r$  direction, m/s;  $v_{g\theta}$  and  $v_{w\theta}$  are the flow velocity of gas and water in the  $\theta$  direction, m/s.

The hydrate in the reservoirs is considered to be solid and immobile, allowing only methane gas and water to seep through the porous media. According to the assumption above, the seepage of gas and water accords with Darcy's theory. The flow velocities of gas

and water in the radial direction ( $r$ ) and circumferential direction ( $\theta$ ) in the porous media can be calculated.  $v_{gr}$ ,  $v_{g\theta}$ ,  $v_{wr}$ , and  $v_{w\theta}$  are determined as follows:

$$v_{gr} = -\frac{KK_g}{\mu_g} \frac{\partial(P_g + \rho_g g \sin(\theta)r)}{\partial r} \quad (5)$$

$$v_{g\theta} = -\frac{KK_g}{\mu_g} \frac{\partial(P_g + \rho_g g \sin(\theta)r)}{r\partial\theta} \quad (6)$$

$$v_{wr} = -\frac{KK_w}{\mu_w} \frac{\partial(P_w + \rho_w g \sin(\theta)r)}{\partial r} \quad (7)$$

$$v_{w\theta} = -\frac{KK_w}{\mu_w} \frac{\partial(P_w + \rho_w g \sin(\theta)r)}{r\partial\theta} \quad (8)$$

where  $g$  is gravitational acceleration,  $m/s^2$ ;  $P_w$ , and  $P_g$  represent the pressure of water and gas, respectively, MPa;  $K$  represents the absolute permeability, mD which is calculated according to Masuda's permeability model [45];  $K_w$  and  $K_g$  represent relative permeabilities of water and gas, respectively;  $K_w$  and  $K_g$  are calculated according to the Stone model [46], as follows:

$$K = k_{do}(1 - S_h)^N \quad (9)$$

$$k_g = \left[ \frac{\bar{S}_G - S_{irG}}{1 - S_{irG}} \right]^{N_g} \quad (10)$$

$$k_w = \left[ \frac{S - S_{irA}}{1 - S_{irA}} \right]^{N_w} \quad (11)$$

where  $k_{do}$  represents the intrinsic permeability of non-hydrate reservoirs, mD;  $N$  is the index of permeability decline;  $S_{irg}$  is the residual saturation of gas, which is set at 0.03 in this model;  $S_{irw}$  is the residual saturation of liquid, which is set at 0.3 in this model;  $N_g$  and  $N_w$  are Corey indexes, which are set at 3.5 and 5, respectively, in this model.

The saturation of gas, water, and hydrates satisfy the following equation:

$$S_g + S_w + S_h = 1 \quad (12)$$

The pressures of gas and water in the porous medium are given by

$$p_{cap} = p_g - p_w \quad (13)$$

where  $P_{cap}$  is the pore capillary pressure. In this model, the calculation equation of the capillary pressure model proposed by Van Genuchten [47] is adopted as follows:

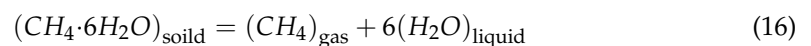
$$p_{cap} = -P_0 \left[ (S^*)^{-\frac{1}{\lambda}} - 1 \right]^{1-\lambda} \quad (14)$$

$$S^* = (S_A - S_{irA}) / S_{mxA} - S_{irA} \quad (15)$$

where  $P_0$  is the initial capillary pressure, namely atmospheric pressure, which is set at 0.1 MPa in this model;  $\lambda$  is the Van Genuchten index, which is set at 0.45 in this model.

### 3.2. Kinetic Model of Hydrate Dissociation and Formation

Hydrate is composed of water molecules and methane molecules. In this model, the dissociation and synthesis reaction of type I methane hydrate are adopted, and the expression is as follows:



Kim and Bishnoi established a kinetic model for the dissociation of NGH. According to the Kim-Bishnoi empirical formula [48], the dissociation rate of methane gas can be calculated as follows:

$$\dot{m}_{gd} = M_g k_d A_s (P_e - P_g) \quad (17)$$

where  $A_s$  is the dissociation specific area of the NGH dissociation surface,  $\text{m}^2/\text{m}^3$ , which is calculated by using the specific surface area formula established by Moridis et al. [49];  $k_d$  is the dissociation constant of the hydrate,  $\text{mol}/(\text{m}^2 \cdot \text{MPa} \cdot \text{s})$ ;  $f_g$  is the methane fugacity on the surface of the hydrate, MPa;  $f_e$  is the methane fugacity under the phase equilibrium pressure, MPa; and  $n_h$  is a function of the number of moles of methane in the hydrate.  $P_g$  is the pressure of methane gas at the local position, MPa;  $P_e$  is the phase equilibrium pressure of methane gas, MPa; and  $\dot{m}_{gd}$  is the dissociation rate of the hydrate,  $\text{kg}/\text{m}^3$ , while the gas hydrate dissociation constant  $k_d$  is calculated using the formula in the Kim and Bishnoi model as follows:

$$A_s = \left[ \frac{(1 - \varphi)}{(4/3)\pi r_p^3} \right] (4\pi r_p^2) (S_h)^{2/3} \quad (18)$$

$$r_p = \left[ 45K(1 - \varphi)^2 / \varphi^3 \right]^{1/2} \quad (19)$$

$$k_d = k_0 \exp\left(-\frac{\Delta E_a}{RT_e}\right) \quad (20)$$

where the basic reaction kinetic constant  $k_0$  is  $3.6 \times 10^4 \text{ mol}/(\text{m}^2 \cdot \text{MPa} \cdot \text{s})$ ;  $\Delta E_a$  is the activation energy of gas hydrate dissociation, J/mol;  $R$  is the universal gas constant, J/(mol·K); according to the simulation calculation in the relevant literature [50], the value of  $\Delta E_a/R$  is 9752.73.

The formation rate of hydrate will be calculated according to the equation given by Mmendra et al. [51] which simulates the process of methane gas combining with water to form NGH, and assumes that the hydrate particles formed are spherical. The final formation rate equation of hydrate is as follow:

$$\dot{m}_{gf} = M_g k_f A_p (P_g - P_e) \quad (21)$$

where  $\dot{m}_{gf}$  is the formation rate of hydrate ( $\text{kg}/\text{m}^3 \cdot \text{s}$ ).  $k_f$  is the formation rate constant of NGH, which is taken as the average measurement value of Englezos et al. [52], namely  $0.5875 \times 10^{-11} \text{ mol}/(\text{m}^2 \cdot \text{MPa} \cdot \text{s})$ ;  $A_p$  is the specific area of the NGH formation surface, ( $\text{m}^2/\text{m}^3$ ), which is calculated as follows according to the relevant literature [53]:

$$A_p = \sqrt{\frac{\varphi^3 (S_w + S_g)^3}{2K}} (S_w S_g S_h)^{2/3} \quad (22)$$

According to the chemical formulas of methane hydrate dissociation reaction and formation reaction, the relationship between the dissociation or production amount of methane hydrate  $m_h$  per unit time and the water consumption or water production amount of dissociation  $m_w$  and gas amount  $m_g$  is as follows:

$$m_h = \frac{M_g + n_w M_w}{M_g} m_g \quad (23)$$

$$m_w = \frac{n_w M_w}{M_g} m_g \quad (24)$$

### 3.3. Energy Transfer in Hydrate Reservoirs

During the drilling of the fluid intruding into the hydrate reservoir, the heat transfer is under the control of heat conduction and heat convection. The process includes heat injection and outflow of drilling fluid, and heat absorption and the heat release of the



dissociation and formation of NGH. Therefore, the conservation equation of energy is described by the temperature change of the hydrate reservoir and the enthalpy change of dissociation and formation of NGH as follows:

$$\frac{1}{r} \frac{\partial}{\partial r} \left( r \lambda_c \frac{\partial T}{\partial r} \right) + \frac{1}{r} \frac{\partial}{\partial \theta} \left( \lambda_c \frac{\partial T}{r \partial \theta} \right) - \frac{\partial}{\partial r} \{ r (\rho_g C_g T v_{gr} + \rho_w C_w T v_{wr}) \} - \frac{1}{r} \frac{\partial}{\partial \theta} (\rho_g C_g T v_{g\theta} + \rho_w C_w T v_{w\theta}) - \dot{m}_h \Delta H = \frac{\partial (T C_t)}{\partial t} \quad (25)$$

$$C_t = (1 - \varphi) \rho_r C_r + \varphi (S_w \rho_w C_w + S_g \rho_g C_g + S_h \rho_h C_h) \quad (26)$$

$$\lambda_c = 1 - \varphi \lambda_r + \varphi (S_w \lambda_w + S_g \lambda_g + S_h \lambda_h) \quad (27)$$

where  $T$  is temperature, K;  $\lambda_g$ ,  $\lambda_w$ ,  $\lambda_h$ , and  $\lambda_r$  are the heat conductivity coefficients of water, gas, NGH, and the hydrate sediments' geotechnical framework, respectively, W/(m·K);  $C_g$ ,  $C_w$ ,  $C_h$ , and  $C_r$  are the heat capacities of gas, water, NGH, and the hydrate sediments' geotechnical framework, respectively, kJ/(kg·K);  $\Delta H$  is the dissociation enthalpy of methane hydrate, kJ/mol;  $\lambda_c$  is the general thermal conductivity of NGH sediments, W/(m·K).

### 3.4. Solving the Numerical Model

The numerical model established in this study includes the processes of mass and heat transfer, gas–liquid two-phase flow, and hydrate dissociation and formation. To solve this model, the finite difference method is used to calculate and solve all discrete equations. The calculation process of the specific model and the discretization and solving process of the equation are shown in Appendix A.

#### 3.4.1. Meshing of Physical Model

Based on the characteristic parameters of the actual hydrate reservoir in the Shenhu area of the South China Sea, this study established a physical model for horizontal well drilling in hydrate reservoirs and conducted drilling operations at different locations within the reservoir (NGH layer center, mixing layer center, and junction of NGH layer and mixing layer), as depicted in Figure 3.

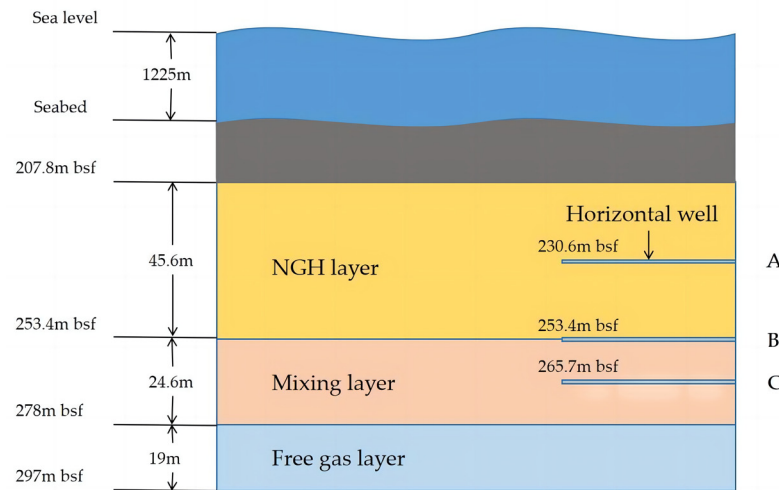


**Figure 3.** Distribution of reservoir types and drilling locations.

In this study, a two-dimensional polar coordinate numerical model of the horizontal well drilling process in hydrate reservoirs is established, with the wellbore with a radius of 0.1 m as the model center to simulate drilling fluid invasion. The grid is divided around the wellbore into radial and circumferential directions. The grid diagram is shown in Figure 4. Because of symmetry, only half of the simulation domain is studied to accelerate computing speed. Circumferential direction is 180°, divided into 20 uniform grids. Radial grid is divided into 50 gradual grids, where the grid spacing  $\Delta r$  is calculated as follows:

$$\Delta r = 0.01 \times 1.05^N \quad (28)$$

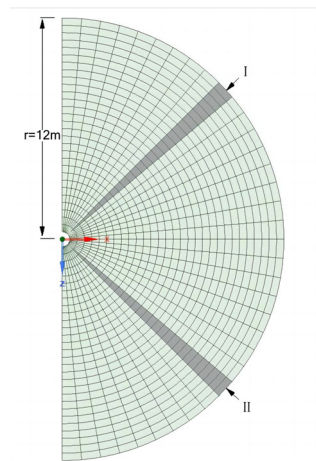


**Figure 4.** Meshing diagram.

### 3.4.2. Boundary Conditions

The initial values for the calculation in this study need to set the relevant parameters of methane hydrate reservoir and borehole drilling fluid, mainly including the initial pressure, initial temperature, permeability, porosity, salinity, saturation of every phase of the hydrate reservoir, as well as the temperature, pressure, density, thermal conductivity, and specific heat capacity of drilling fluid.

The initial values of temperature and pressure of the NGH reservoir are determined considering the geothermal gradient and pressure gradient of the actual hydrate sediment:

$$T = T_0 + t_g r \sin \theta \quad (29)$$

$$P = P_0 + p_g r \sin \theta \quad (30)$$

where  $t_g$  is the low temperature gradient, K/m;  $p_g$  is the pressure gradient, MPa/m.

The numerical model of horizontal well drilling in the NGH reservoir established in this work is a two-dimensional polar coordinate model. Since the reservoir only has vertical physical property differences and the physical properties at the same height are the same, the model structure is a horizontally symmetric semicircle for the sake of convenience in calculation, as shown in Figure 4. The main boundary conditions have two parts: one is the internal boundary at the wellbore; the other is the outer boundary of the NGH reservoir on the far side. For the internal boundary, the relevant parameters are regarded as the first type of boundary conditions:

$$T = T_f, P = P_f, S_h = 0, S_g = 0, S_w = 1, X_s = X_{sf} (r = r_w) \quad (31)$$

For the outer boundary, it is set as an infinite extension boundary because the calculation range is much larger than the invasion range of drilling fluid. Therefore, the temperature and pressure of the NGH reservoir are considered as the first type of boundary conditions, so the temperature of the outer boundary is kept constant:

$$T = T_0, P = P_0 (r = R) \quad (32)$$

## 4. Results

### 4.1. Physical Properties of Hydrate Reservoirs during Horizontal Well Drilling

#### 4.1.1. Two-Dimensional Physical Response of Hydrate Reservoir

In the drilling process of the horizontal well, due to the effects of temperature and pressure gradients of the hydrate reservoir and different reservoir permeabilities, significant differences arise in the changes of physical properties around the wellbore and hydrate dissociation behaviors [29,35]. Therefore, in this study, we focus on location B to illustrate

these changes in hydrate reservoirs, which is at the junction of the NGH layer and mixing layer (location B in Figure 3). In the simulation, the drilling fluid temperature is set as 16 °C and the pressure is 15.34 MPa. Other parameters are used in Table 1.

Figure 5 gives the distribution of reservoir physical properties at the 24th hour. Figure 5a–f are the distributions of pressure, temperature, hydrate saturation, gas saturation, water saturation, and salinity of the pore water.

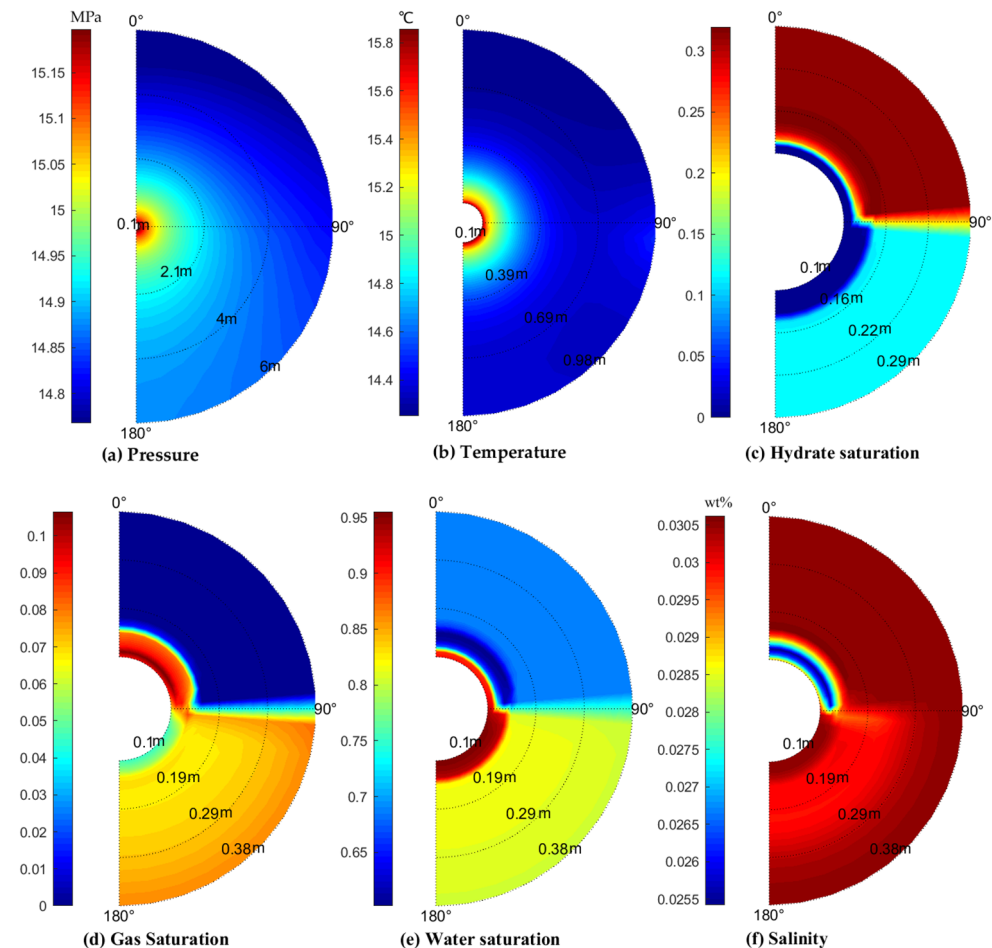


**Figure 5.** Reservoir physical property distributions at the 24th hour in the NGH layer + mixing layer.

As shown in Figure 5a,b, the pressure of drilling fluid is higher than that of the reservoir, leading to the drilling fluid invading into the hydrate reservoir and displacing the primary fluid (gas and water) in the reservoir near the wellbore, resulting in an increase in pore pressure near the wellbore, which then transfers continuously to areas farther from the wellbore. Within a radius of about 2 m from the center of the well, the reservoir pressure significantly increases, while beyond this distance, the pressure increases slightly, and approaches the initial reservoir pressure. It can also be seen from Figure 4a that the pressure in the mixing layer is slightly higher than that in the NGH layer. In the simulation, the hydrate saturation of the NGH layer (the upper part of Figure 5a–f) is 0.31, with a permeability of 2.38 mD, while the hydrate saturation of the mixing layer (the lower part of Figure 5a–f) is 0.117, with a permeability of 6.63 mD. Due to the higher permeability of the mixing layer, the fluid seepage effect is stronger, resulting in a faster pressure transfer. As shown in Figure 5b, the initial temperature of the reservoir is lower than that of drilling fluid. Consequently, under the effect of heat conduction and convection between the drilling fluid and hydrate reservoir, the temperature noticeably increases near the wellbore. This temperature rise mainly occurs within a range of about 0.39 m from the center of the

wellbore, which is much smaller than that of the pressure increase, indicating that the speed of temperature propagation is much lower than that of the pressure.

Figure 5c shows the distribution of the hydrate saturation. It can be seen that due to the rapid increases in temperature and pressure near the wellbore, which break the hydrate stability, the hydrate saturation significantly changes in the region near the wellbore and represents different behaviors in the NGH layer and mixing layer. The hydrate close to the wellbore has completely decomposed, as shown in the blue area in Figure 5c. This phenomenon occurs in both the NGH layer and mixing layer. Following this, partial hydrate dissociation occurs in areas where the temperature increase rate is lower than the pressure increase rate. Notably, the extent of hydrate dissociation in the mixing layer is much larger than that in the NGH layer. This may be due to the lower hydrate saturation and higher permeability of the mixing layer, facilitating a greater intrusion of drilling fluid. In addition, hydrate secondary formation occurs in the NGH layer, leading to the formation of a zone with high hydrate saturation, which further inhibits the drilling fluid invasion.

Figure 5d,e give the distributions of the gas and liquid saturation, respectively. The significant production of water and methane gas resulting from hydrate dissociation and drilling fluid invasion causes notable changes in gas and water saturations near the wellbore. Furthermore, these saturations are influenced by secondary hydrate formation. As shown in Figure 5d,e, the distributions of gas and water saturation exhibit substantial differences between the NGH layer and the mixing layer due to various complex factors. In the NGH layer, where there is originally no free gas, the hydrate dissociation of hydrate results in considerable increases in both gas and water saturations. Particularly, water saturation significantly increases near the wellbore and decreases rapidly as far away from the wellbore. Due to the hydrate secondary formation, there is a region with water saturation lower than the initial value. In the mixing layer, characterized by a low initial hydration saturation of 0.117 and a high permeability of 6.63 mD, the quantity of gas produced from hydrate dissociation is much lower compared to that in the NGH layer. Furthermore, there is no secondary hydrate formation. As the hydrate dissociation occurs, the size and the number of channels increase, and the flow capacity of the water increases [54]. Consequently, a large amount of drilling fluid invades and displaces the pore fluid (gas, water) of the reservoir, resulting in an increase in water saturation and a decrease in gas saturation.

The salinity of pore water in the reservoir is significantly affected by hydrate dissociation, hydrate formation, and the invasion of drilling fluid [36]. Figure 5f indicates the distribution of the pore water salinity, revealing significant differences between the NGH layer and mixing layer. In the NGH layer, pore water salinity in the near-wellbore area significantly decreases due to hydrate dissociation, which produces a large amount of water, diluting the salinity of pore water. In the secondary hydrate formation zone, the salinity of pore water rises due to water consumption by secondary hydrate formation. In the mixing layer, the pore water salinity remains relatively consistent with the initial salinity near the wellbore, and then there is a large area with the low salinity due to the dilution effect by hydrate dissociation. Meanwhile, the low-salinity area is larger than the hydrate dissociation area. This is because the water was dissociated from the hydrate and was moved far away by the drilling fluid invasion, which can be seen from the gas and water distributions. Overall, in the NGH layer, the salinity of the pore water is mainly influenced by the dissociation of hydrate and secondary hydrate formation. In the mixing layer, due to the lower hydrate saturation and the greater invasion of drilling fluid, the salinity of the pore water is mainly influenced by the drilling fluid invasion and the hydrate dissociation in the NGH reservoir.

#### 4.1.2. Curves of Changes in Properties of Hydrate Reservoir at Different Time

To better demonstrate the variation of physical properties in different hydrate layers during horizontal drilling, Figure 6 exhibits the changes over time at different distances from the wellbore. The data were obtained from reservoir locations at angles of 45 °C and 135 °C of location B, as shown in Figure 4. It can be seen from Figure 6a that the pressure



propagation rate in the mixing layer is slightly higher than that in the NGH layer, due to the influence of the pressure gradient of the reservoir. Similarly, Figure 6b shows that the temperature propagation rate in the mixing layer is also higher than that in the NGH layer. This difference arises from the influence of the geothermal gradient, resulting in slightly higher temperatures in the mixing layer compared to the NGH layer at positions farther from the wellbore. Notably, while pressure can spread to a radius of about 8 m, the temperature propagation is limited to a radius of about 0.8 m.

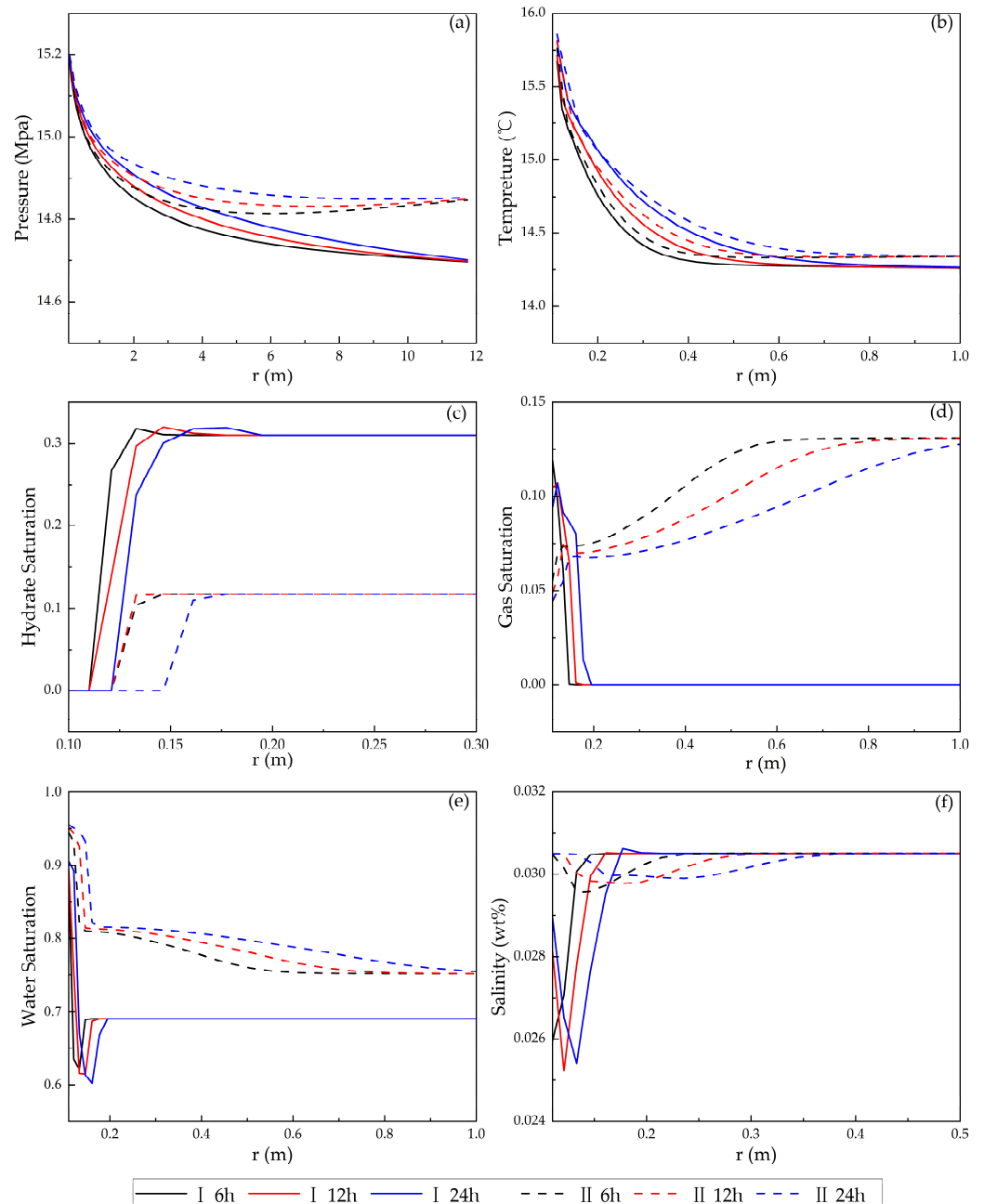


**Figure 6.** Curves of physical properties of hydrate reservoir changing with time during drilling. (a) Pressure; (b) temperature; (c) hydrate saturation; (d) gas saturation; (e) water saturation; (f) salinity.

Figure 6c shows the variation in hydrate saturation over time during the drilling process. As shown in Figure 6c, the area of the hydrate dissociation in the mixing layer is much larger than that in the NGH layer. At the 24th hour, the complete dissociation zone of the NGH layer reaches a radius of about 0.125 m, while in the mixing layer, it reaches a

radius of about 0.15 m. The hydrate dissociation area gradually expands with the drilling time in both the NGH layer and the mixing layer.

Figure 6d,e presents the curves of gas and water saturations at different times, respectively. The gas and water saturations of the reservoir around the wellbore are affected by hydrate dissociation and formation, drilling fluid invasion, and gas–liquid seepage in the reservoir. In both the NGH layer and mixing layer, the water saturation increases in the area around the wellbore due to hydrate dissociation and drilling fluid invasion. In the NGH layer, an obvious decrease in water saturation occurs due to hydrate secondary formation, which consumes water. As the drilling becomes longer and longer, the area with the low water saturation becomes larger, which is in line with the area of the hydrate secondary formation. In the mixing layer, the water saturation near the wellbore is very high, and the gas saturation is lower than the initial saturation. This is because the drilling fluid invasion displaces pore fluid, causing the water saturation near the wellbore to be higher. After passing the hydrate dissociation zone, the displacement effect greatly attenuates and the gas–liquid seepage is the main effect, so the gas–liquid saturation changes gradually to the original gas–liquid saturation. Comparing the gas–liquid saturation curves of the NGH layer and the mixing layer, it can be clearly seen that the gas–liquid flow in the mixing layer is relatively violent, and the drilling fluid invasion is serious.

In the study, the drilling fluid salinity is same as the original pore water salinity, which is 3.05 wt%. Therefore, the salinity of the pore water is mainly affected by hydrate dissociation and secondary formation. Figure 6f shows that the salinities of pore water in the NGH layer and mixing layer both decrease firstly and then increase. The decrease in the salinity is due to the hydrate dissociation, which produces a lot of water, diluting the reservoir pore water. As the drilling fluid invades, the salinity near the wellbore will rise. In the NGH layer, the hydrate dissociation makes the salinity decrease to the lowest salinity of 2.54 wt%. A region with a higher salinity than the initial value of the reservoir can be seen in the salinity curve. This is because the secondary formation of hydrate consumes part of the water in the NGH layer. In the mixing layer, due to the smaller amount of hydrate dissociation and no secondary formation of hydrate, a relatively flat low-salinity area is observed around the wellbore. The lowest salinity of the mixing layer is 2.97 wt%, which is significantly higher than that of the NGH layer. With the increase in time, both in the NGH layer and mixing layer, the range of low-salinity area gradually expands and moves away from the well.

#### 4.2. Comparison of Hydrate Dissociation at Different Locations of the Reservoir

The above analysis shows that the NGH layer and mixing layer have great differences in the hydrate dissociation and the change in physical properties due to the differences in permeability and hydrate/gas/water saturations in the original reservoir. In order to further study the hydrate dissociation characteristics of the reservoir during horizontal drilling at different drilling locations, simulations were conducted at three different locations: the center of the NGH layer, the junction of the NGH layer and the mixing layer, the center of the mixing layer, respectively, denoted as locations A, B, and C in Figure 3. These locations are located at depths of 230.6 m, 253.4 m, and 265.7 m below the seabed, respectively. Other specific parameters are shown in Table 1.

Figure 7 gives the distribution of the hydrate saturation at different drilling locations at the 12th and 24th hour of drilling. From Figure 7, it can be seen that the hydrate distributions in both the NGH layer and mixing layer are basically the same as the upper part and lower part of location B, as detailed in Figure 5c. In all three locations, the dissociation and the formation zones gradually move farther away. Comparing Figure 7d,f, it can be seen that the secondary formation area of the NGH layer in Figure 7d appears darker, with the highest hydrate saturation reaching 0.35, which is higher than that in Figure 7f. This disparity arises because location A is positioned higher than location B, resulting in a lower initial temperature and pressure of the reservoir due to pressure and temperature gradients. During the drilling process, the pressure transfer is rapid while

the temperature transfer is slow, resulting in the pressure of the hydrate reservoir at two locations being similar. Under the same pressure, the lower temperature promotes the secondary hydrate formation, resulting in the higher secondary formation saturation at location A. Comparing Figure 7e,f, it also can be seen that the hydrate dissociation range at location C is larger than that of the mixing layer part at location B. This is also caused by the difference in initial temperature at different reservoir heights. The reservoir at location B has a slightly higher temperature, which is more conducive to hydrate dissociation.

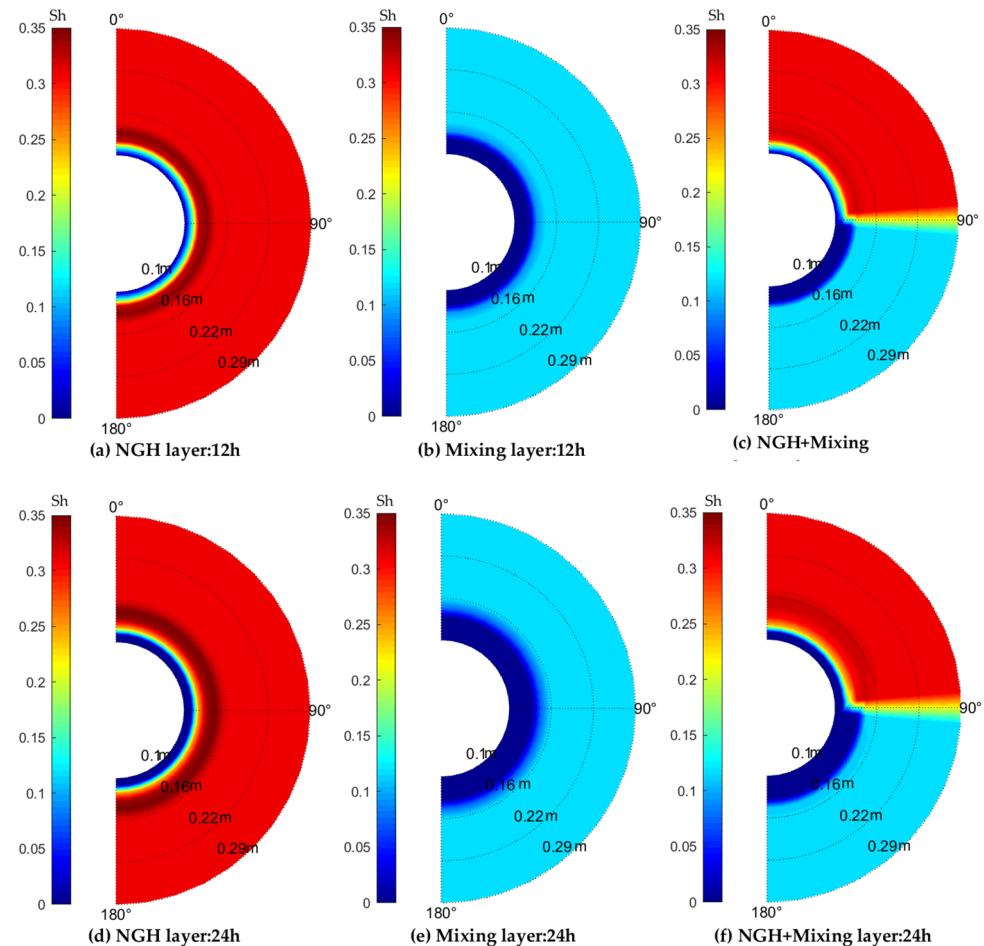


**Figure 7.** Comparison of hydrate saturation distribution at different locations at the 12th hour and 24th hour. (a) NGH layer at the 12th hour; (b) mixing layer at the 12th hour; (c) NGH layer and mixing layer at the 12th hour; (d) NGH layer at the 24th hour; (e) mixing layer at the 24th hour; (f) NGH layer and mixing layer at the 24th hour.

As analyzed above, the differences in the hydrate/gas saturations and permeability of the reservoir lead to significant differences in drilling invasion and hydrate dissociation among different reservoir layers. The change in pore pressure caused by the drilling fluid invasion and the degradation of reservoir strength resulting from hydrate dissociation has significant impacts on the wellbore stability [25]. Therefore, although the hydrate production using horizontal wells in the hydrate reservoir with high permeability can enhance gas production efficiency to some extent, the drilling process may lead to a large amount of hydrate dissociation surrounding the wellbore, which is not conducive to wellbore stability and drilling safety. In addition, at the conjunction of the NGH layer and mixing layer, due to the different hydrate dissociation rate above and below the wellbore, the difference change in stress at different regions around the wellbore can also induce the instability of the wellbore.

To better compare the difference of the drilling invasion and hydrate dissociation at different locations in the reservoir during horizontal well drilling, the amounts of hydrate dissociation and the drilling fluid invasion (per meter of horizontal well) at different times were calculated, which are given in Figure 8. It can be seen from Figure 7 that the hydrate dissociation ranges at different locations are mainly concentrated in the range of 0.25 m from the center of the wellbore. Therefore, the hydrate dissociation amount within a 0.25 m radius is calculated.

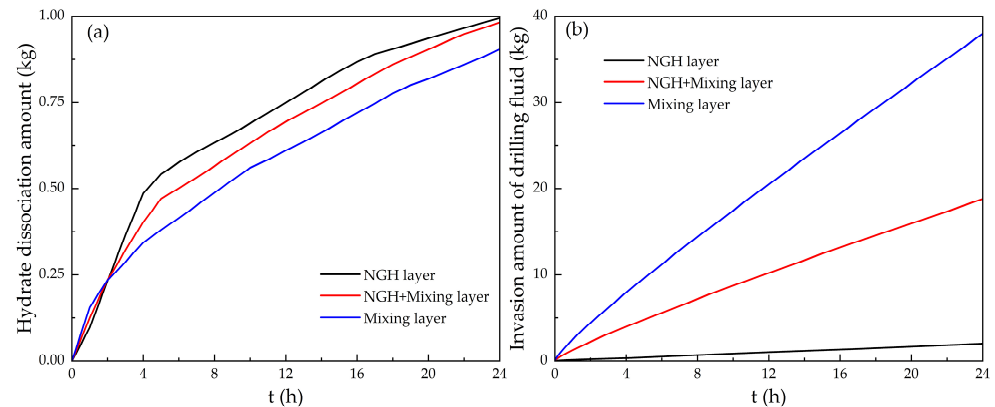


**Figure 8.** Curves of hydrate dissociation amount and drilling fluid invasion amount at different locations changing with time. (a) Hydrate dissociation amount; (b) drilling fluids invasion amount.

Figure 8a indicates that the hydrate dissociation rates at different locations all increase rapidly at early stages of the drilling. Within the first 2 h, location A shows the smallest amount of hydrate dissociation. In the NGH layer, the hydrate saturation is much higher than that in the mixing layer, and more hydrate will be dissociated by the heat transfer from the drilling fluid at an early stage. Figure 8b shows the curves of the amount of the drilling fluid invasion into the reservoir over time for a unit length of the horizontal well. The drilling fluid invasion increases linearly with time, and the invasion amount at location C is much greater than that at location A, and the invasion amount at the junction of the hydrate and mixing layers (location B) is between them. At the 24th hour, the invasion amount of drilling fluid at location C in the mixing layer reaches about 38 kg, while at location A in the NGH layer, it is only 2.02 kg. The invasion amount of drilling fluid in the mixing layer is about 18.8 times more than that in the NGH layer. Therefore, it can be speculated that hydrate dissociation is mainly driven by heat conducted from the drilling fluid to the reservoir. Similar findings were reported by Sun et al. [42]; they indicated that hydrate dissociation is mainly derived from heat conduction caused by the temperature difference between the wellbore and reservoir, especially in regions with high water saturation. For the mixing layer, even the hydrate saturation is much lower than the NGH layer, due to the high invasion amount of drilling fluid, as shown in Figure 8b, with the more heat brought by the invaded drilling fluid, the amount of dissociated hydrate at location C is a little higher than that at location A. As the drilling progresses, the heat from the drilling fluid is consumed by the hydrate dissociation, and cannot be directly transferred to the region far from the wellbore. The amount of dissociated hydrate gradually decreases to be lower than that at location A after about the 2nd hour. However, the hydrate dissociation rate at location A also significantly drops at about the 4th hour. Due to the expansion of the hydrate dissociation range, the effect of the heat conduction from the wellbore on the hydrate dissociation also decreases. After the 4th hour, the secondary hydrate gradually increases, the difference in the amount of dissociated hydrate between the NGH layer and the mixing layer is gradually maintained to basically become stable. Because the hydrate dissociation amount is affected by the hydrate saturation in the reservoir, although the hydrate invasion amount in the mixing layer is significantly higher than that in the NGH layer, the hydrate dissociation amount does not present a great change. As shown



in Figure 8b, at the 24th hour, the hydrate dissociation amount is 0.995 kg at location A, 0.905 kg at location C, and 0.981 kg at location B. Under the high invasion of the drilling fluid, the hydrate dissociation amount in the mixing layer is similar to that of the NGH layer even though the initial hydrate saturation of the NGH layer was 2.65 times that of the mixing layer. It can be concluded that in the NGH layer with no free gas and low permeability, the hydrate dissociation is mainly caused by the heat conduction. In the mixing layer, the effect of the drilling fluid invasion exerts greater impact on the hydrate dissociation, resulting in the amount of hydrate dissociation slightly lower than that in the NGH layer with a much higher hydrate saturation.

#### 4.3. Influence of Salinity

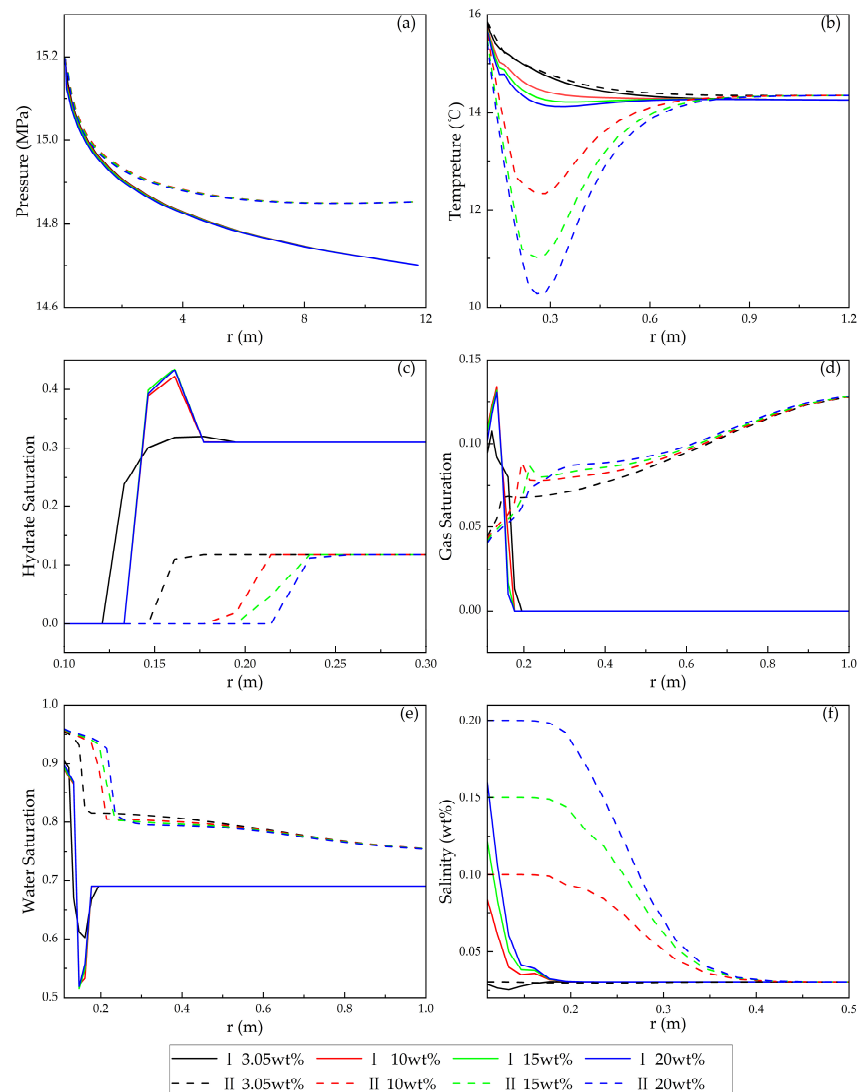
In the drilling process, in order to prevent the secondary formation of hydrate in the wellbore, it is necessary to increase the salinity of drilling fluid or add hydrate inhibitors to decrease the equilibrium temperature of hydrate formation [28]. However, during drilling fluid invasion, higher drilling fluid salinity can promote the hydrate dissociation in reservoirs. Therefore, the simulation of hydrate dissociation behaviors under different salinities of the drilling fluid at location B in Figure 3 was conducted. The drilling fluid salinities used were 3.05 wt%, 10 wt%, 15 wt%, and 20 wt%.

Figure 9 shows the physical properties of the reservoir near the wellbore at the 24th hour under different drilling fluid salinities. The data were obtained from reservoir locations at angles of 45 °C and 135 °C of location B, as shown in Figure 4. As shown in Figure 9a, the salinity of the drilling fluid has almost no effect on the pressure distribution. However, with the increase in the drilling fluid salinity, the temperature near the wellbore slightly decreases in the NGH layer and drops drastically in the mixing layer. This is because the drilling fluid invasion in the NGH layer promotes the hydrate dissociation, especially in the mixing layer with a large amount of the drilling fluid invasion. Under the high salinity of 20 wt%, the minimum temperature of the low-temperature area is close to 10 °C, which is lower than the initial reservoir temperature by 4 °C.

As shown in Figure 9c, the salinity of the drilling fluid has an important impact on the hydrate dissociation. In the NGH layer, higher salinity levels increase the extent of the complete dissociation zone of hydrate and promote secondary hydrate formation. With the increase in salinity from 3.05 wt% to 20 wt%, the hydrate dissociation range in the mixing layer increases from 0.16 m to 0.23 m, while the hydrate dissociation range in the NGH layer does not significantly change. This may be because under the higher salinity, the invasion of drilling fluid promotes the dissociation of hydrate in the near-wellbore area. However, due to the low permeability of the reservoir, much gas dissociated from hydrate accumulates in the periphery of the hydrate dissociation area, forming abundant secondary hydrate, further reducing the permeability of the reservoir, preventing the further invasion of drilling fluid. In the mixing layer, due to the high permeability of the reservoir, there is no secondary formation area of hydrate under the higher salinity, so the complete dissociation zone of hydrate gradually becomes larger with the increase in salinity. This also causes the rapid expansion of the low-temperature area of the mixing layer and the sharp drop in temperature in Figure 9b.

As shown in Figure 9d,e, the changes of drilling fluid salinity also lead to changes in gas and water saturations. In the NGH layer, gas and water saturations are relatively less affected by the drilling fluid salinity. In the mixing layer, due to the existence of free gas and a higher salinity, the hydrate dissociation area expands, and the drilling fluid invades faster, resulting in higher water saturation around the wellbore. Meanwhile, the free gas and hydrate dissociation gas in the reservoir flow away, causing the change to gas saturation in the area far from the wellbore. Figure 9f describes the changes in the pore water salinity under different drilling fluid salinities. When the drilling fluid salinity increases, the salinity of the pore water near the wellbore in the NGH layer also increases. However, due to the influence of the secondary formation of hydrate, the drilling fluid invades a smaller range, and the pore water salinity rapidly decreases to the initial salinity.

In the mixing layer, the drilling fluid invades a wider range, and the salinity diffusion range increases to the radius of about 0.4 m, while the salinity diffusion range of the NGH layer is less than the radius of about 0.2 m.

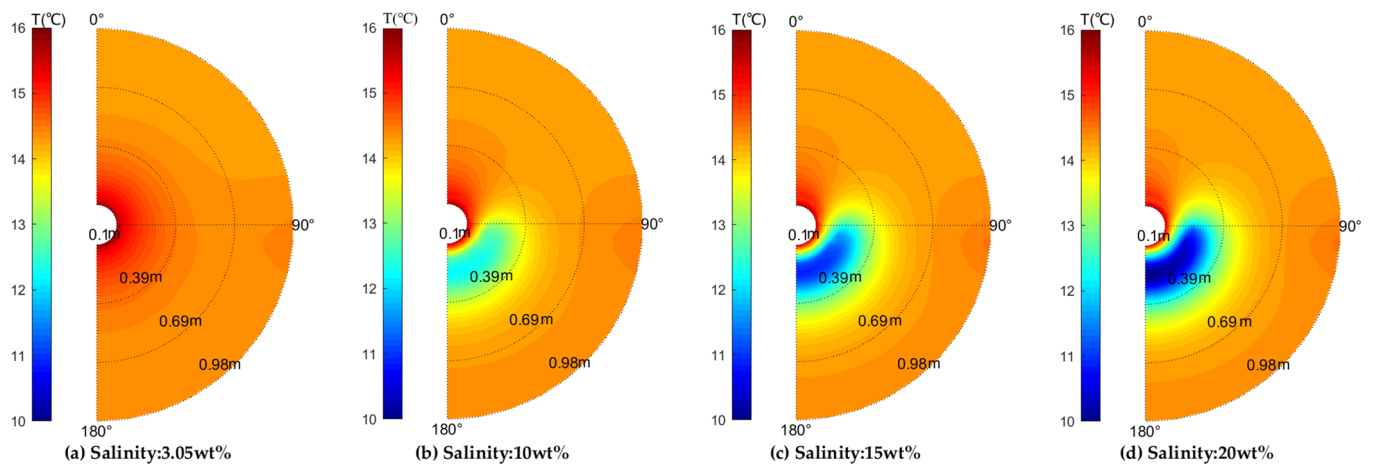


**Figure 9.** Changes in physical properties under different drilling fluid salinity conditions. (a) Pressure; (b) temperature; (c) hydrate saturation; (d) gas saturation; (e) water saturation; (f) salinity.

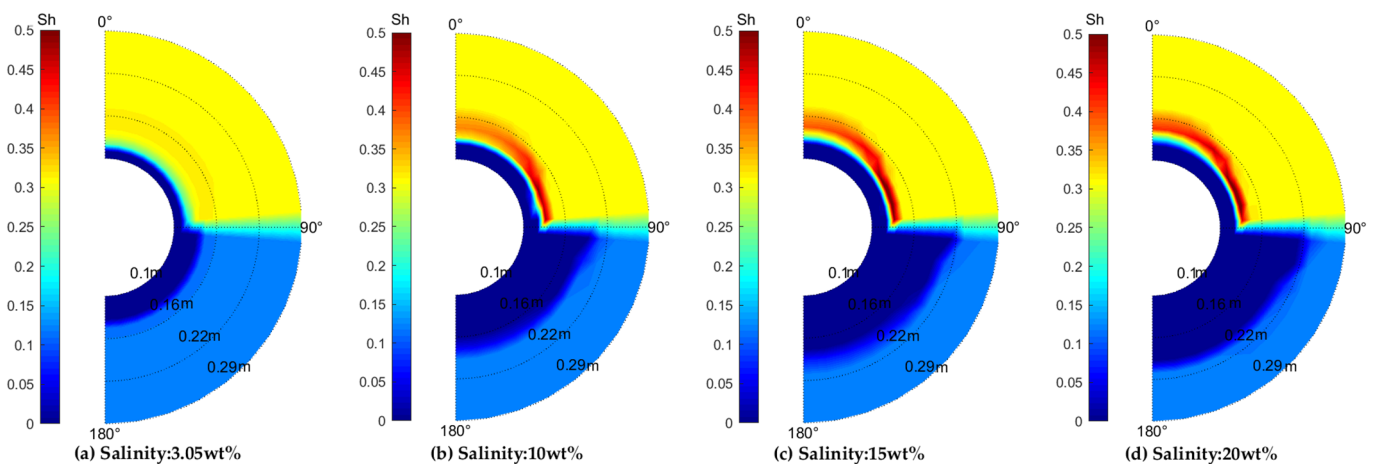
Figure 10 shows the temperature distributions of the hydrate reservoir with different drilling fluid salinities at the 24th hour. It can be clearly seen that under the high salinity, a wide range of the low-temperature area appears in the mixing layer, which even affects the NGH layer. With the continuous increase in salinity, the range of the low-temperature area expands, and the minimum temperature of the low-temperature area keeps decreasing.

Figure 11 describes the distribution of hydrate saturation with various drilling fluid salinities. As shown in Figure 11, with the increase in salinity, the hydrate dissociation range expands significantly in the mixing layer and slightly in the NGH layer. In the NGH layer, the amount and range of the secondary formation hydrate noticeably increase with salinity increases from 3.05 wt% to 10 wt%, and then have little change with further increases. Sun et al. [42] found that increasing the drilling fluid salinity slightly accelerates the hydrate dissociation around the wellbore of the reservoir with high water saturation, and the effects on the wellbore stability are negligible. A similar phenomenon is observed in the NGH layer in this study. However, for the mixing layer characterized by free gas and high permeability of the reservoir, the rapid increase in hydrate dissociation with increasing

drilling fluid salinity may significantly increase the risk of wellbore instability. Therefore, it is necessary to have stricter control over the salinity of drilling fluids.



**Figure 10.** Distributions of temperature in the reservoir with different drilling fluid salinities. (a) Salinity at 3.05 wt%; (b) salinity at 10 wt%; (c) salinity at 15 wt%; (d) salinity at 20 wt%.



**Figure 11.** Distributions of hydrate saturation with various drilling fluid salinities. (a) Salinity at 3.05 wt%; (b) salinity at 10 wt%; (c) salinity at 15 wt%; (d) salinity at 20 wt%.

## 5. Discussion

### 5.1. Novelities and Suggestions

Both scientific research and actual exploitation show that horizontal wells can improve the efficiency of NGH exploitation. However, drilling horizontal wells in deep water hydrate deposits is a challenging task. The drilling process is very important to ensure the safe and continuous exploitation of hydrates. However, there is a lack of research on the drilling process of horizontal wells, especially for different hydrate reservoir types and properties. In this study, a two-dimensional polar coordinate numerical model is established to simulate and analyze the hydrate formation and dissociation around the wellbore, and drilling fluid invasion characteristics of the horizontal well drilling process in high-permeability hydrate containing free gas and low-permeability hydrate without free gas. At the same time, the influence of drilling fluid salinity on the hydrate dissociation in different reservoir types is studied.

Due to the complexity of reservoir structures, the reservoir characteristics will significantly change during horizontal drilling, such as hydrate saturation, permeability, and free gas content. It is necessary to clarify the dissociation of hydrate around the wellbore and its control mechanism in horizontal drilling under different reservoir characteristics, which is

the prerequisite for ensuring the safe and controllable implementation of the drilling process. In this study, by comparing horizontal drilling in the NGH layer and mixing layer, we found that in the mixing layer with low hydrate saturation and high permeability, drilling fluid invasion is serious and causes large-scale hydrate dissociation; on the contrary, in the NGH layer with high hydrate saturation and low permeability, the drilling fluid invasion is small and the scope of hydrate dissociation is small. At the same time, the formation of a high-hydrate saturation zone due to the secondary formation of hydrate is conducive to mitigate drilling fluid invasion. Therefore, it is recommended that the horizontal well is located in the area with high hydrate saturation in the reservoir, which is conducive to mitigate the degree of drilling fluid invasion and reduce the risk of well wall instability.

The increase in drilling fluid salinity will promote the dissociation of the reservoir hydrate at the well wall, resulting in the collapse of hydrate cemented mud and sand particles, sharply reducing the mechanical strength of the surrounding rock of the well wall, and causing well instability problems [28]. In the mixing layer, the higher drilling fluid salinity will cause the significant expansion of the hydrate dissociation area, while in the NGH layer, the influence of drilling fluid salinity on the scope of hydrate dissociation is relatively weak. Therefore, in the drilling process of reservoirs containing free gas and low hydrate saturation, it is necessary to control the parameters such as drilling fluid salinity to more strictly evaluate the impact of hydrate dissociation on the stability of the reservoir and wellbore.

The results of this numerical simulation study can provide certain guidance for the well deployment position and the adjustment of drilling fluid parameters in the future drilling process of NGH horizontal wells, provide certain suggestions for the safety of drilling process, and have important significance for ensuring the safety of NGH exploitation.

## 5.2. Limitations and Future Work

In the drilling process, the well wall instability caused by hydrate dissociation is the main reason for drilling safety. The dissociation of hydrate in sediments will cause the change in sediment mechanical strength and pore structure. Hydrate has a cementing effect and skeleton-supporting effect on sediment particles. When the hydrate is decomposed into fluid, the loss of its cementing effect and skeleton-supporting effect leads to the transformation of skeleton sand to flow sand. Furthermore, it reduces the mechanical strength of the reservoir, leading to formation subsidence and even well wall collapse. In the process of horizontal well drilling, due to the differences in the properties of the reservoir above and below the wellbore, different hydrate dissociation and mechanical characteristics change the laws occurring above and below the wellbore, so the horizontal well drilling needs a stricter evaluation of the stability of the reservoir and the wellbore. In this work, the impact of hydrate dissociation characteristics caused by heat and mass transfer between the wellbore and the reservoir is investigated. In the future work, the change in reservoir mechanical characteristics and pore structure should be further considered, and the drilling simulation model of coupling geomechanics should be established to better carry out the evaluation of the wellbore stability in the process of horizontal well drilling. In addition, the actual hydrate reservoir usually has complex geological conditions and hydrate distribution. At present, due to the lack of geological exploration technology, the actual specific parameters and distribution characteristics of the hydrate reservoir are not clear. In the numerical simulation of hydrate drilling and mining, the average parameters are usually used for reservoir properties, such as porosity, hydrate saturation, and permeability. Because the horizontal well has a longer drilling distance, the heterogeneity of the hydrate reservoir should be further considered, and a three-dimensional hydrate drilling model that conforms to the actual reservoir should be constructed in order to evaluate the safety of the entire drilling process. In addition, based on the clear distribution characteristics of specific parameters in hydrate reservoirs, besides drilling processes, attention should be paid to the modeling of three-dimensional comprehensive hydrate systems, such as these



studies documenting stability [55], evolution [56,57], and the destabilization [58] of gas hydrates at basin scales [59,60].

## 6. Conclusions

In this study, a two-dimensional polar coordinate numerical model was established to simulate the physical response characteristics of NGH reservoirs during horizontal well drilling. Based on the properties of the second production test area in the Shenhu area of the South China Sea, the hydrate dissociation and physical properties of the hydrate reservoir with different characteristics were simulated, and the effect of drilling fluid salinity on the hydrate dissociation was investigated. The following conclusions were drawn:

- (1) During the horizontal well drilling process, significant changes occur in distributions of temperature, pressure, saturation, and salinity in the reservoir around the wellbore. Temperature and pressure exhibit rapid responses over a wide range, and pressure exhibits a faster transmission rate and greater range compared to temperature. The pressure and temperature transmission rates in the mixing layer are higher than those in the NGH layer.
- (2) The rapid changes in pressure and temperature result in extensive hydrate dissociation around the wellbore. The area of the hydrate dissociation in the mixing layer is much larger than that in the NGH layer, which may lead to the increase in risk of wellbore instability. In the NGH layer, there is a zone of secondary hydrate formation on the periphery of the hydrate dissociation zone, which inhibits the drilling fluid invasion.
- (3) The drilling fluid invasion in the mixing layer is much higher than that in the NGH layer due to the higher permeability and lower hydrate saturation. The invasion amount of drilling fluid in the mixing layer is 18.8 times more than that in the NGH layer. Under the high invasion of the drilling fluid, the hydrate dissociation amount in the mixing layer is similar to that of the NGH layer even though the initial hydrate saturation of the NGH layer was 2.65 times that of the mixing layer. The hydrate dissociation is mainly caused by the heat conduction between the wellbore and the reservoir in the NGH layer, and by the heat convection by the drilling fluid invasion in the mixing layer. The drilling fluid invasion combined with the hydrate dissociation and formation affects the distributions of gas, water, and salinity of the pore water around the wellbore, which presents significantly different changes in behaviors in the NGH layer and mixing layer.
- (4) The drilling fluid salinity has less influence on hydrate dissociation near the wellbore in the NGH layer compared with that in the mixing layer due to the less drilling fluid invasion. With the increase in salinity from 3.05 wt% to 20 wt%, the hydrate dissociation range in the mixing layer increases from 0.16 m to 0.23 m, while the hydrate dissociation range in the NGH layer does not significantly change. In the NGH layer, the hydrate dissociation and secondary formation are promoted when the salinity increases from 3.05 wt% to 10 wt%, and then doesn't change much as the salinity further increases. In the mixing layer, the hydrate dissociation keeps increasing as the salinity of the drilling fluid increase, leading to range extension of low-temperature area and the lowest temperature (down to 10 °C, which is lower than the initial reservoir temperature by 4 °C). In the mixing layer, it is significant to control the drilling fluid salinity in a reasonable range to ensure the stability of the wellbore.

**Author Contributions:** Conceptualization, F.G. and Y.Z.; methodology, Y.Z.; software, F.G. and Y.Z.; investigation, F.G. and C.C.; writing—original draft preparation, F.G.; writing—review and editing, Y.Z. and C.C.; supervision, X.L. and Z.C.; funding acquisition, X.L. All authors have read and agreed to the published version of the manuscript.

**Funding:** This research was funded by the National Natural Science Foundation of China (52076208 and 51736009), Guangdong Special Support Program—Local Innovation and Entrepreneurship Team Project (2019BT02L278), Special Project for Marine Economy Development of Guangdong Province

(GDME-2022D043, GDME-2020D044, GDNRC [2022]45) and the National Key R&D Program of China (2021YFC2800902), which are gratefully acknowledged.

**Institutional Review Board Statement:** Not applicable.

**Informed Consent Statement:** Not applicable.

**Data Availability Statement:** Data are contained within the article.

**Conflicts of Interest:** The authors declare no conflicts of interest.

## Appendix A

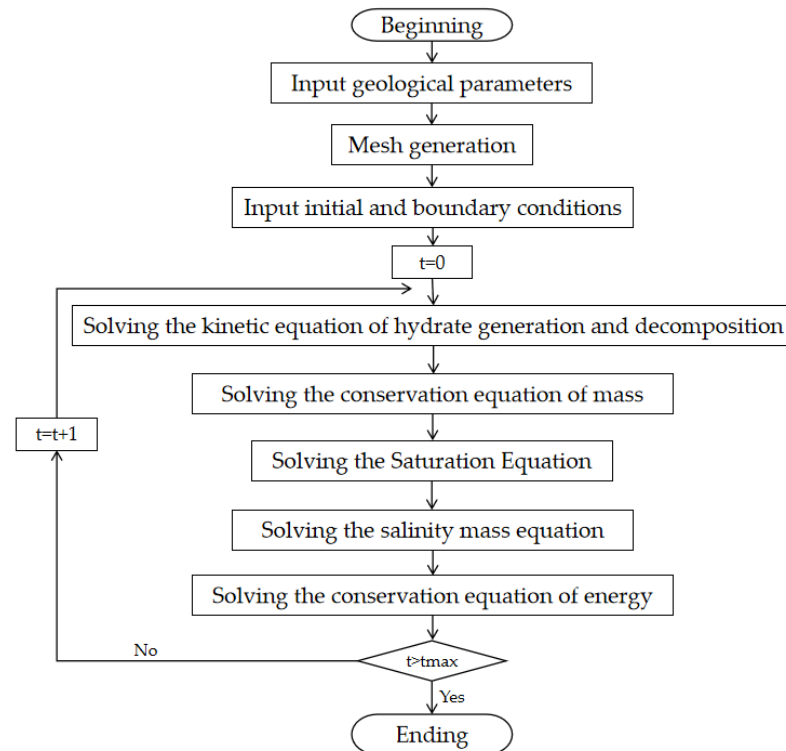


**Figure A1.** Procedure flow chart of numerical solution.

Substitute Darcy's equation of seepage velocity into the original equation of mass conservation:

Gas phase:

$$\frac{1}{r} \frac{\partial}{\partial r} \left( r \rho_g \frac{KK_g}{\mu_g} \frac{\partial (P_g + \rho_w g \sin(\theta) r)}{\partial r} \right) + \frac{1}{r} \frac{\partial}{\partial \theta} \left( \rho_g \frac{KK_g}{\mu_g} \frac{\partial (P_g + \rho_w g \sin(\theta) r)}{r \partial \theta} \right) + \dot{m}_g M_g = \varphi \rho_g \frac{\partial (S_g)}{\partial t} + S_g \rho_g (\varphi C_g + C_r) \frac{\partial P}{\partial t} \quad (A1)$$

Liquid phase:

$$\frac{1}{r} \frac{\partial}{\partial r} \left( r \rho_w \frac{KK_w}{\mu_w} \frac{\partial (P_w + \rho_w g \sin(\theta) r)}{\partial r} \right) + \frac{1}{r} \frac{\partial}{\partial \theta} \left( \rho_w \frac{KK_w}{\mu_w} \frac{\partial (P_w + \rho_w g \sin(\theta) r)}{r \partial \theta} \right) + \dot{m}_w M_w = \varphi \rho_w \frac{\partial (S_w)}{\partial t} + S_w \rho_w (\varphi C_w + C_r) \frac{\partial P}{\partial t} \quad (A2)$$

Hydrate phase:

$$\varphi \rho_h \frac{\partial (S_h)}{\partial t} = -\dot{m}_h (M_g + n_w M_w) \quad (A3)$$

The above equation was respectively dispersed by the finite difference in the implicit forward difference scheme. Subscript “*i*” (node position) and superscript “*n* + 1” (unknown time layer) of pressure and saturation terms in the difference equation were omitted, and the difference equation was obtained as follows:

Gas phase:

$$\begin{aligned} & \frac{1}{r_i} \left\{ \frac{\left( \frac{KK_g}{\mu_g} \right)_{i-1} \rho_{g(i-1)} r_{i-1} \frac{(P_g + \rho_{gg} \sin(\theta) r)_{i-1} - (P_g + \rho_{gg} \sin(\theta) r)_i}{\Delta r_i} - \left( \frac{KK_g}{\mu_g} \right)_i \rho_g r_i \frac{(P_g + \rho_{gg} \sin(\theta) r)_i - (P_g + \rho_{gg} \sin(\theta) r)_{i+1}}{\Delta r_{i+1}}}{\frac{\Delta r_i + \Delta r_{i+1}}{2}} \right\} \\ & + \frac{1}{r_i} \left\{ \frac{\left( \frac{KK_g}{\mu_g} \right)_{j-1} \rho_{g(j-1)} \frac{(P_g + \rho_{gg} \sin(\theta) r)_{j-1} - (P_g + \rho_{gg} \sin(\theta) r)_j}{r_i \Delta \theta} - \left( \frac{KK_g}{\mu_g} \right)_j \rho_{gj} \frac{(P_g + \rho_{gg} \sin(\theta) r)_j - (P_g + \rho_{gg} \sin(\theta) r)_{j+1}}{r_i \Delta \theta}}{\Delta \theta} \right\} \\ & + \dot{m}_g M_g = \varphi \rho_g \left( \frac{S_g - S_g^n}{\Delta t} + S_g^n (C_{pg} + C_{pr} / \varphi) \frac{P_g - P_g^n}{\Delta t} \right) \end{aligned} \quad (A4)$$

Liquid phase:

$$\begin{aligned} & \frac{1}{r_i} \left\{ \frac{\left( \frac{KK_w}{\mu_w} \right)_{i-1} \rho_{w(i-1)} r_{i-1} \frac{(P_w + \rho_{wg} \sin(\theta) r)_{i-1} - (P_w + \rho_{wg} \sin(\theta) r)_i}{\Delta r_i} - \left( \frac{KK_w}{\mu_w} \right)_i \rho_w r_i \frac{(P_w + \rho_{wg} \sin(\theta) r)_i - (P_w + \rho_{wg} \sin(\theta) r)_{i+1}}{\Delta r_{i+1}}}{\frac{\Delta r_i + \Delta r_{i+1}}{2}} \right\} \\ & + \frac{1}{r_i} \left\{ \frac{\left( \frac{KK_w}{\mu_w} \right)_{j-1} \rho_{w(j-1)} \frac{(P_w + \rho_{wg} \sin(\theta) r)_{j-1} - (P_w + \rho_{wg} \sin(\theta) r)_j}{r_i \Delta \theta} - \left( \frac{KK_w}{\mu_w} \right)_j \rho_{wj} \frac{(P_w + \rho_{wg} \sin(\theta) r)_j - (P_w + \rho_{wg} \sin(\theta) r)_{j+1}}{r_i \Delta \theta}}{\Delta \theta} \right\} \\ & + \dot{m}_w M_w = \varphi \rho_w \left( \frac{S_w - S_w^n}{\Delta t} + S_w^n (C_{pw} + C_{pr} / \varphi) \frac{P_w - P_w^n}{\Delta t} \right) \end{aligned} \quad (A5)$$

Hydrate phase:

$$\varphi r_i \Delta \theta \frac{\Delta r_i + \Delta r_{i+1}}{2} \rho_h \frac{S_h - S_h^n}{\Delta t} = -r_i \Delta \theta \frac{\Delta r_i + \Delta r_{i+1}}{2} m_h (M_g + n_w M_w) \quad (A6)$$

Darcy's equation was substituted into the energy conservation equation and differentially discretized. The temperature control equation was solved by explicit forward differential scheme for the thermal conductivity phase and by explicit upwind differential scheme for the convection term. The differential equations were obtained as follows:

$$\begin{aligned} & \frac{1}{r_i} \left\{ \frac{r_{i-1} \lambda_{i-1} \frac{T_{i-1} - T_i}{\Delta r_i} - r_i \lambda_i \frac{T_i - T_{i+1}}{\Delta r_{i+1}}}{\frac{\Delta r_i + \Delta r_{i+1}}{2}} \right\} + \frac{1}{r_i} \left\{ \frac{\lambda_{j-1} \frac{T_{j-1} - T_j}{\Delta \theta} - \lambda_j \frac{T_j - T_{j+1}}{\Delta \theta}}{r \Delta \theta} \right\} \\ & \frac{1}{r_i} \left\{ \frac{\left( \frac{KK_g}{\mu_g} \right)_{i-1} \rho_{g(i-1)} r_{i-1} C_g T_{i-1} \frac{(P_g + \rho_{gg} \sin(\theta) r)_{i-1} - (P_g + \rho_{gg} \sin(\theta) r)_i}{\Delta r_i} - \left( \frac{KK_g}{\mu_g} \right)_i \rho_g r_i C_g T_i \frac{(P_g + \rho_{gg} \sin(\theta) r)_i - (P_g + \rho_{gg} \sin(\theta) r)_{i+1}}{\Delta r_{i+1}}}{\frac{\Delta r_i + \Delta r_{i+1}}{2}} \right\} \\ & \frac{1}{r_i} \left\{ \frac{\left( \frac{KK_w}{\mu_w} \right)_{i-1} \rho_{w(i-1)} r_{i-1} C_w T_{i-1} \frac{(P_w + \rho_{wg} \sin(\theta) r)_{i-1} - (P_w + \rho_{wg} \sin(\theta) r)_i}{\Delta r_i} - \left( \frac{KK_w}{\mu_w} \right)_i \rho_w r_i C_w T_i \frac{(P_w + \rho_{wg} \sin(\theta) r)_i - (P_w + \rho_{wg} \sin(\theta) r)_{i+1}}{\Delta r_{i+1}}}{\frac{\Delta r_i + \Delta r_{i+1}}{2}} \right\} \\ & + \frac{1}{r_i} \left\{ \frac{\left( \frac{KK_g}{\mu_g} \right)_{j-1} \rho_{g(j-1)} C_g T_{j-1} \frac{(P_g + \rho_{gg} \sin(\theta) r)_{j-1} - (P_g + \rho_{gg} \sin(\theta) r)_j}{r_i \Delta \theta} - \left( \frac{KK_g}{\mu_g} \right)_j \rho_{gj} C_g T_j \frac{(P_g + \rho_{gg} \sin(\theta) r)_j - (P_g + \rho_{gg} \sin(\theta) r)_{j+1}}{r_i \Delta \theta}}{\Delta \theta} \right\} \\ & \frac{1}{r_i} \left\{ \frac{\left( \frac{KK_w}{\mu_w} \right)_{j-1} \rho_{w(j-1)} C_w T_{j-1} \frac{(P_w + \rho_{wg} \sin(\theta) r)_{j-1} - (P_w + \rho_{wg} \sin(\theta) r)_j}{r_i \Delta \theta} - \left( \frac{KK_w}{\mu_w} \right)_j \rho_{wj} C_w T_j \frac{(P_w + \rho_{wg} \sin(\theta) r)_j - (P_w + \rho_{wg} \sin(\theta) r)_{j+1}}{r_i \Delta \theta}}{\Delta \theta} \right\} \\ & - \dot{m}_h (M_g + n_w M_w) \Delta H = \frac{C_t T - (C_t T)^n}{\Delta t} \end{aligned} \quad (A7)$$

Substitute Darcy's equation into the salinity mass conservation equation, and carry out explicit finite difference separation, and the difference equation is as follows:

$$\begin{aligned}
& \frac{1}{r_i} \left\{ \frac{\left( \frac{KK_w}{\mu_w} \right)_{i-1} r_{i-1} (X_{s(i-1)})^n \frac{(P_w + \rho_w g \sin(\theta) r)_{i-1} - (P_w + \rho_w g \sin(\theta) r)_i}{\Delta r_i} - \left( \frac{KK_w}{\mu_w} \right)_i r_i (X_s)^n \frac{(P_w + \rho_w g \sin(\theta) r)_{i-1} - (P_w + \rho_w g \sin(\theta) r)_{i+1}}{\Delta r_{i+1}}}{\frac{\Delta r_i + \Delta r_{i+1}}{2}} \right\} \\
& + \frac{1}{r_i} \left\{ \frac{\left( \frac{KK_w}{\mu_w} \right)_{j-1} (X_{s(j-1)})^n \frac{(P_w + \rho_w g \sin(\theta) r)_{j-1} - (P_w + \rho_w g \sin(\theta) r)_j}{r_i \Delta \theta} - \left( \frac{KK_w}{\mu_w} \right)_j (X_s)^n \frac{(P_w + \rho_w g \sin(\theta) r)_{j-1} - (P_w + \rho_w g \sin(\theta) r)_{j+1}}{r_i \Delta \theta}}{\Delta \theta} \right\} \\
& + K_{DD} \frac{1}{r_i} \left\{ \frac{r_{i-1} (\varphi_{i-1} S_w)^n \frac{X_{s(i-1)} - X_s}{\Delta r_i} - r_i (\varphi S_w)^n \frac{X_s - X_{s(i+1)}}{\Delta r_{i+1}}}{\frac{\Delta r_i + \Delta r_{i+1}}{2}} \right\} + K_{DD} \frac{1}{r_i} \left\{ \frac{(\varphi_{j-1} S_w)^n \frac{X_{s(j-1)} - X_s}{r_i \Delta \theta} - (\varphi S_w)^n \frac{X_s - X_{s(j+1)}}{r_i \Delta \theta}}{\Delta \theta} \right\} \\
& = \frac{X_s \varphi S_w - (X_s \varphi S_w)^n}{\Delta t}
\end{aligned} \quad (A8)$$

In the previous article, according to the hydrate formation and dissociation rate equation and the hydrate mass conservation equation, the hydrate saturation at the next moment is calculated as follows:

$$S_h = S_h^n - \dot{m}_h \frac{\Delta t}{\varphi \rho_h} \quad (A9)$$

The simultaneous mass conservation equations of gas, liquid, and hydrate phases were used to eliminate the saturation of gas, liquid, and hydrate in the unknown time layer. Then, the gas pressure was converted into liquid pressure phase through the capillary pressure equation. Finally, the LU dissociation method was used to solve the equation to obtain the liquid pressure distribution at the next moment.

$$\begin{aligned}
& \left( \frac{KK_g}{\mu_g} \right)_{i-1} \frac{\rho_g(i-1)}{\rho_g} r_{i-1} \Delta \theta \frac{(P_g(i-1) - P_g)}{\Delta r_i} - \frac{KK_g}{\mu_g} r_i \Delta \theta \frac{(P_g - P_{g(i+1)})}{\Delta r_{i+1}} \\
& + \left( \frac{KK_g}{\mu_g} \right)_{i-1} \frac{\rho_g(i-1)}{\rho_g} r_{i-1} \Delta \theta \frac{\rho_g(i-1) r_{i-1} - \rho_g r_i}{\Delta r_i} g \sin(\theta) - \frac{KK_g}{\mu_g} r_i \Delta \theta \frac{\rho_g r_i - \rho_{g(i+1)} r_{i+1}}{\Delta r_i} g \sin(\theta) \\
& + \left( \frac{KK_g}{\mu_g} \right)_{j-1} \frac{\rho_g(j-1)}{\rho_g} \frac{\Delta r_i + \Delta r_{i+1}}{2} \frac{(P_g(j-1) - P_g)}{r_i \Delta \theta} - \left( \frac{KK_g}{\mu_g} \right) \frac{\Delta r_i + \Delta r_{i+1}}{2} \frac{(P_g - P_{g(j+1)})}{r_i \Delta \theta} \\
& + \left( \frac{KK_g}{\mu_g} \right)_{j-1} \frac{\rho_g(j-1)}{\rho_g} \frac{\Delta r_i + \Delta r_{i+1}}{2} g \frac{\rho_g(j-1) \sin(\theta_{j-1}) - \rho_g \sin(\theta_j)}{\Delta \theta} - \left( \frac{KK_g}{\mu_g} \right) \frac{\Delta r_i + \Delta r_{i+1}}{2} g \frac{\rho_g \sin(\theta_j) - \rho_{g(j+1)} \sin(\theta_{j+1})}{\Delta \theta} \\
& + \left( \frac{KK_w}{\mu_w} \right)_{i-1} \frac{\rho_w(i-1)}{\rho_w} r_{i-1} \Delta \theta \frac{(P_w(i-1) - P_w)}{\Delta r_i} - \frac{KK_w}{\mu_w} r_i \Delta \theta \frac{(P_g - P_{g(i+1)})}{\Delta r_{i+1}} \\
& + \left( \frac{KK_w}{\mu_w} \right)_{i-1} \frac{\rho_w(i-1)}{\rho_w} r_{i-1} \Delta \theta \frac{\rho_w(i-1) r_{i-1} - \rho_w r_i}{\Delta r_i} g \sin(\theta) - \frac{KK_w}{\mu_w} r_i \Delta \theta \frac{\rho_w r_i - \rho_{w(i+1)} r_{i+1}}{\Delta r_i} g \sin(\theta) \\
& + \left( \frac{KK_w}{\mu_w} \right)_{j-1} \frac{\rho_w(j-1)}{\rho_w} \frac{\Delta r_i + \Delta r_{i+1}}{2} \frac{(P_w(j-1) - P_w)}{r_i \Delta \theta} - \left( \frac{KK_w}{\mu_w} \right) \frac{\Delta r_i + \Delta r_{i+1}}{2} \frac{(P_w - P_{w(j+1)})}{r_i \Delta \theta} \\
& + \left( \frac{KK_w}{\mu_w} \right)_{j-1} \frac{\rho_w(j-1)}{\rho_w} \frac{\Delta r_i + \Delta r_{i+1}}{2} g \frac{\rho_w(j-1) \sin(\theta_{j-1}) - \rho_w \sin(\theta_j)}{\Delta \theta} - \left( \frac{KK_w}{\mu_w} \right) \frac{\Delta r_i + \Delta r_{i+1}}{2} g \frac{\rho_w \sin(\theta_j) - \rho_{w(j+1)} \sin(\theta_{j+1})}{\Delta \theta} \\
& + r_i \Delta \theta \frac{\Delta r_i + \Delta r_{i+1}}{2} m_g \frac{M_g}{\rho_g} + r_i \Delta \theta \frac{\Delta r_i + \Delta r_{i+1}}{2} m_w \frac{M_w}{\rho_w} - r_i \Delta \theta \frac{\Delta r_i + \Delta r_{i+1}}{2} m_h \frac{M_h}{\rho_h} \\
& = \varphi r_i \Delta \theta \frac{\Delta r_i + \Delta r_{i+1}}{2} \left( S_g^n (C_{pg} + C_{pr} / \varphi) \frac{P_g - P_g^n}{\Delta t} + S_w^n (C_{pw} + C_{pr} / \varphi) \frac{P_w - P_w^n}{\Delta t} \right)
\end{aligned} \quad (A10)$$

In the difference equation of mass conservation in the liquid phase, the pressure of the unknown time layer is known, and only the water saturation of the next time layer is unknown. Then, the difference equation of mass conservation in the liquid phase is directly solved to obtain the water saturation:

$$\begin{aligned}
& \left( \frac{KK_w}{\mu_w} \right)_{i-1} \frac{\rho_w(i-1)}{\rho_w} r_{i-1} \Delta \theta \frac{(P_w(i-1) - P_w)}{\Delta r_i} - \frac{KK_w}{\mu_w} r_i \Delta \theta \frac{(P_w - P_{w(i+1)})}{\Delta r_{i+1}} \\
& + \left( \frac{KK_w}{\mu_w} \right)_{i-1} \frac{\rho_w(i-1)}{\rho_w} r_{i-1} \Delta \theta \frac{\rho_w(i-1) r_{i-1} - \rho_w r_i}{\Delta r_i} g \sin(\theta) - \frac{KK_w}{\mu_w} r_i \Delta \theta \frac{\rho_w r_i - \rho_{w(i+1)} r_{i+1}}{\Delta r_i} g \sin(\theta) \\
& + \left( \frac{KK_w}{\mu_w} \right)_{j-1} \frac{\rho_w(j-1)}{\rho_w} \frac{\Delta r_i + \Delta r_{i+1}}{2} \frac{(P_w(j-1) - P_w)}{r_i \Delta \theta} - \left( \frac{KK_w}{\mu_w} \right) \frac{\Delta r_i + \Delta r_{i+1}}{2} \frac{(P_w - P_{w(j+1)})}{r_i \Delta \theta} \\
& + \left( \frac{KK_w}{\mu_w} \right)_{j-1} \frac{\rho_w(j-1)}{\rho_w} \frac{\Delta r_i + \Delta r_{i+1}}{2} g \frac{\rho_w(j-1) \sin(\theta_{j-1}) - \rho_w \sin(\theta_j)}{\Delta \theta} - \left( \frac{KK_w}{\mu_w} \right) \frac{\Delta r_i + \Delta r_{i+1}}{2} g \frac{\rho_w \sin(\theta_j) - \rho_{w(j+1)} \sin(\theta_{j+1})}{\Delta \theta} \\
& + r_i \Delta \theta \frac{\Delta r_i + \Delta r_{i+1}}{2} m_w \frac{M_w}{\rho_w}
\end{aligned} \left\{ \div \left( \varphi r_i \Delta \theta \frac{\Delta r_i + \Delta r_{i+1}}{2} \right) \right. \quad (A11)$$

According to the reservoir pressure and phase saturation distribution obtained in the previous section, the equation is directly solved to obtain the salinity distribution of the hydrate reservoir:

$$\begin{aligned}
& \left[ \begin{aligned}
& \left( \frac{KK_w}{\mu_w} \right)_{i-1} r_{i-1} \Delta \theta \left( X_{s(i-1)} \right)^n \frac{P_{w(i-1)} - P_w}{\Delta r_i} - \left( \frac{KK_w}{\mu_w} \right)_i r_i \Delta \theta \left( X_s \right)^n \frac{P_w - P_{w(i+1)}}{\Delta r_{i+1}} \\
& + \left( \frac{KK_w}{\mu_w} \right)_{i-1} r_{i-1} \Delta \theta \left( X_{s(i-1)} \right)^n \frac{\rho_{w(i-1)} r_{i-1} - \rho_w r_i}{\Delta r_i} g \sin(\theta) - \left( \frac{KK_w}{\mu_w} \right)_i r_i \Delta \theta \left( X_s \right)^n \frac{\rho_w r_i - \rho_{w(i+1)} r_{i+1}}{\Delta r_{i+1}} g \sin(\theta) \\
& + \left( \frac{KK_w}{\mu_w} \right)_{j-1} \frac{\Delta r_i + \Delta r_{i+1}}{2} \left( X_{s(j-1)} \right)^n \frac{P_{w(j-1)} - P_w}{r_i \Delta \theta} - \left( \frac{KK_w}{\mu_w} \right)_j \frac{\Delta r_i + \Delta r_{i+1}}{2} \left( X_s \right)^n \frac{P_w - P_{w(j+1)}}{r_i \Delta \theta} \\
& + \left( \frac{KK_w}{\mu_w} \right)_{j-1} \frac{\Delta r_i + \Delta r_{i+1}}{2} \left( X_{s(j-1)} \right)^n g \frac{\rho_{w(i-1)} \sin(\theta_{j-1}) - \rho_w \sin(\theta)}{\Delta \theta} - \left( \frac{KK_w}{\mu_w} \right)_j \frac{\Delta r_i + \Delta r_{i+1}}{2} \left( X_s \right)^n g \frac{\rho_w \sin(\theta) - \rho_{w(i+1)} \sin(\theta_{j+1})}{\Delta \theta} \\
& + r_{i-1} \Delta \theta \left( \varphi_{i-1} S_{w(i-1)} \right)^n K_{DD} \frac{X_{s(i-1)} - X_s}{\Delta r_i} - r_i \Delta \theta \left( \varphi S_w \right)^n K_{DD} \frac{X_s - X_{s(i+1)}}{\Delta r_{i+1}} \\
& + \frac{\Delta r_i + \Delta r_{i+1}}{2} \left( \varphi_{j-1} S_{w(j-1)} \right)^n K_{DD} \frac{X_{s(j-1)} - X_s}{r_i \Delta \theta} - \frac{\Delta r_i + \Delta r_{i+1}}{2} \left( \varphi S_w \right)^n K_{DD} \frac{X_s - X_{s(j+1)}}{r_i \Delta \theta} \\
& + \frac{\Delta r_i + \Delta r_{i+1}}{2} r_i \Delta \theta \frac{(X_s \varphi S_w)^n}{\Delta t}
\end{aligned} \right] \\
X_s = & \frac{\Delta r_i + \Delta r_{i+1}}{2} r_i \Delta \theta \varphi S_w
\end{aligned} \quad (A12)$$

Finally, the LU dissociation method is used to solve the energy conservation equation again, and the reservoir temperature distribution is obtained:

$$\begin{aligned}
& \lambda_{i-1} r_{i-1} \Delta \theta \frac{T_{i-1} - T_i}{\Delta r_i} - \lambda_i r_i \Delta \theta \frac{T_i - T_{i+1}}{\Delta r_{i+1}} + \lambda_{j-1} \frac{\Delta r_i + \Delta r_{i+1}}{2} \frac{T_{j-1} - T_j}{r_i \Delta \theta} - \lambda_j \frac{\Delta r_i + \Delta r_{i+1}}{2} \frac{T_j - T_{j+1}}{r_i \Delta \theta} \\
& + \left( \frac{KK_g}{\mu_g} \right)_{i-1} r_{i-1} \Delta \theta \rho_{g(i-1)} C_g T_{i-1} \frac{(P_g + \rho_g g \sin(\theta) r)_{i-1} - (P_g + \rho_g g \sin(\theta) r)_i}{\Delta r_i} - \left( \frac{KK_g}{\mu_g} \right)_i \rho_g r_i \Delta \theta C_g T_i \frac{(P_g + \rho_g g \sin(\theta) r)_i - (P_g + \rho_g g \sin(\theta) r)_{i+1}}{\Delta r_{i+1}} \\
& + \left( \frac{KK_w}{\mu_w} \right)_{i-1} r_{i-1} \Delta \theta \rho_{w(i-1)} C_w T_{i-1} \frac{(P_w + \rho_w g \sin(\theta) r)_{i-1} - (P_w + \rho_w g \sin(\theta) r)_i}{\Delta r_i} - \left( \frac{KK_w}{\mu_w} \right)_i \rho_w r_i \Delta \theta C_w T_i \frac{(P_w + \rho_w g \sin(\theta) r)_i - (P_w + \rho_w g \sin(\theta) r)_{i+1}}{\Delta r_{i+1}} \\
& + \left( \frac{KK_g}{\mu_g} \right)_{j-1} \frac{\Delta r_i + \Delta r_{i+1}}{2} \rho_{g(j-1)} C_g T_{j-1} \frac{(P_g + \rho_g g \sin(\theta) r)_{j-1} - (P_g + \rho_g g \sin(\theta) r)_j}{r_i \Delta \theta} - \left( \frac{KK_g}{\mu_g} \right)_j \frac{\Delta r_i + \Delta r_{i+1}}{2} \rho_{g j} C_g T_j \frac{(P_g + \rho_g g \sin(\theta) r)_j - (P_g + \rho_g g \sin(\theta) r)_{j+1}}{r_i \Delta \theta} \\
& \left( \frac{KK_w}{\mu_w} \right)_{j-1} \frac{\Delta r_i + \Delta r_{i+1}}{2} \rho_{w(j-1)} C_w T_{j-1} \frac{(P_w + \rho_w g \sin(\theta) r)_{j-1} - (P_w + \rho_w g \sin(\theta) r)_j}{r_i \Delta \theta} - \left( \frac{KK_w}{\mu_w} \right)_j \frac{\Delta r_i + \Delta r_{i+1}}{2} \rho_{w j} C_w T_j \frac{(P_w + \rho_w g \sin(\theta) r)_j - (P_w + \rho_w g \sin(\theta) r)_{j+1}}{r_i \Delta \theta} \\
& - \frac{\Delta r_i + \Delta r_{i+1}}{2} r_i \Delta \theta m_h (M_g + n_w M_w) \Delta H = \frac{\Delta r_i + \Delta r_{i+1}}{2} r_i \Delta \theta \frac{C_i T - (C_i T)^n}{\Delta t}
\end{aligned} \quad (A13)$$

The solution results are used to update all parameters (temperature, pressure, various saturation, and salinity) as the initial values of the next time step, and the distribution of the parameters in each time step is calculated iteratively until the set calculation time is completed.

## References

1. Kvenvolden, K.A. Potential Effects of Gas Hydrate on Human Welfare. *Proc. Natl. Acad. Sci. USA* **1999**, *96*, 3420–3426. [CrossRef] [PubMed]
2. Haligva, C.; Linga, P.; Ripmeester, J.A.; Englezos, P. Recovery of Methane from a Variable-Volume Bed of Silica Sand/Hydrate by Depressurization. *Energy Fuels* **2010**, *24*, 2947–2955. [CrossRef]
3. Konno, Y.; Masuda, Y.; Hariguchi, Y.; Kurihara, M.; Ouchi, H. Key Factors for Depressurization-Induced Gas Production from Oceanic Methane Hydrates. *Energy Fuels* **2010**, *24*, 1736–1744. [CrossRef]
4. Fitzgerald, G.C.; Castaldi, M.J.; Zhou, Y. Large Scale Reactor Details and Results for the Formation and Decomposition of Methane Hydrates via Thermal Stimulation Dissociation. *J. Pet. Sci. Eng.* **2012**, *94–95*, 19–27. [CrossRef]
5. Wang, Y.; Li, X.-S.; Li, G.; Huang, N.-S.; Feng, J.-C. Experimental Study on the Hydrate Dissociation in Porous Media by Five-Spot Thermal Huff and Puff Method. *Fuel* **2014**, *117*, 688–696. [CrossRef]
6. Schicks, J.M.; Spangenberg, E.; Giese, R.; Steinhauer, B.; Klump, J.; Luzi, M. New Approaches for the Production of Hydrocarbons from Hydrate Bearing Sediments. *Energies* **2011**, *4*, 151–172. [CrossRef]
7. Chandrasekharan Nair, V.; Mech, D.; Gupta, P.; Sangwai, J.S. Polymer Flooding in Artificial Hydrate Bearing Sediments for Methane Gas Recovery. *Energy Fuels* **2018**, *32*, 6657–6668. [CrossRef]
8. Wang, Y.; Lang, X.; Fan, S.; Wang, S.; Yu, C.; Li, G. Review on Enhanced Technology of Natural Gas Hydrate Recovery by Carbon Dioxide Replacement. *Energy Fuels* **2021**, *35*, 3659–3674. [CrossRef]
9. Kurihara, M.; Yamamoto, K.; Numasawa, M. Analysis of Production Data for 2007/2008 Mallik Gas Hydrate Production Tests in Canada. In Proceedings of the CPS/SPE International Oil & Gas Conference and Exhibition in China, Beijing, China, 8–10 June 2010.
10. Kvamme, B. Thermodynamic Limitations of the CO<sub>2</sub>/N<sub>2</sub> Mixture Injected into CH<sub>4</sub> Hydrate in the Ignik Sikumi Field Trial. *J. Chem. Eng. Data* **2016**, *61*, 1280–1295. [CrossRef]
11. Yamamoto, K.; Kanno, T.; Wang, X.X.; Tamaki, M.; Fujii, T.; Chee, S.S.; Wang, X.W.; Pimenov, V.; Shako, V. Thermal Responses of a Gas Hydrate-Bearing Sediment to a Depressurization Operation. *RSC Adv.* **2017**, *7*, 5554–5577. [CrossRef]
12. Yamamoto, K.; Wang, X.X.; Tamaki, M.; Suzuki, K. The Second Offshore Production of Methane Hydrate in the Nankai Trough and Gas Production Behavior from a Heterogeneous Methane Hydrate Reservoir. *RSC Adv.* **2019**, *9*, 25987–26013. [CrossRef]
13. Li, J.-F.; Ye, J.-L.; Qin, X.-W.; Qiu, H.-J.; Wu, N.-Y.; Lu, H.-L.; Xie, W.-W.; Lu, J.-A.; Peng, F.; Xu, Z.-Q.; et al. The First Offshore Natural Gas Hydrate Production Test in South China Sea. *China Geol.* **2018**, *1*, 5–16. [CrossRef]
14. Ye, J.-L.; Qin, X.-W.; Xie, W.-W.; Lu, H.-L.; Ma, B.-J.; Qiu, H.-J.; Liang, J.-Q.; Lu, J.-A.; Kuang, Z.-G.; Lu, C.; et al. The Second Natural Gas Hydrate Production Test in the South China Sea. *China Geol.* **2020**, *3*, 197–209. [CrossRef]



15. Zhuo, L.; Yu, J.; Zhang, H.; Zhou, C. Influence of Horizontal Well Section Length on the Depressurization Development Effect of Natural Gas Hydrate Reservoirs. *Nat. Gas Ind. B* **2021**, *8*, 505–513. [\[CrossRef\]](#)
16. Feng, J.-C.; Wang, Y.; Li, X.-S.; Li, G.; Zhang, Y.; Chen, Z.-Y. Effect of Horizontal and Vertical Well Patterns on Methane Hydrate Dissociation Behaviors in Pilot-Scale Hydrate Simulator. *Appl. Energy* **2015**, *145*, 69–79. [\[CrossRef\]](#)
17. Feng, Y.; Chen, L.; Suzuki, A.; Kogawa, T.; Okajima, J.; Komiya, A.; Maruyama, S. Numerical Analysis of Gas Production from Layered Methane Hydrate Reservoirs by Depressurization. *Energy* **2019**, *166*, 1106–1119. [\[CrossRef\]](#)
18. Li, G.; Moridis, G.J.; Zhang, K.; Li, X.-S. Evaluation of Gas Production Potential from Marine Gas Hydrate Deposits in Shenhu Area of South China Sea. *Energy Fuels* **2010**, *24*, 6018–6033. [\[CrossRef\]](#)
19. Yang, S.; Lang, X.; Wang, Y.; Wen, Y.; Fan, S. Numerical Simulation of Class 3 Hydrate Reservoirs Exploiting Using Horizontal Well by Depressurization and Thermal Co-Stimulation. *Energy Convers. Manag.* **2014**, *77*, 298–305. [\[CrossRef\]](#)
20. Dong, L.; Wan, Y.; Li, Y.; Liao, H.; Liu, C.; Wu, N.; Leonenko, Y. 3D Numerical Simulation on Drilling Fluid Invasion into Natural Gas Hydrate Reservoirs. *Energy* **2022**, *241*, 122932. [\[CrossRef\]](#)
21. Shang, S.; Gu, L.; Zhan, L.; Qiu, H.; Lu, H. Application of Horizontal Well to Gas Production from a Hydrate Reservoir with Free Gas and High Irreducible Water. *J. Nat. Gas Sci. Eng.* **2021**, *9*, 104102. [\[CrossRef\]](#)
22. Yuan, Y.; Xu, T.; Jin, C.; Zhu, H.; Gong, Y.; Wang, F. Multiphase Flow and Mechanical Behaviors Induced by Gas Production from Clayey-Silt Hydrate Reservoirs Using Horizontal Well. *J. Clean. Prod.* **2021**, *328*, 129578. [\[CrossRef\]](#)
23. Yin, Z.; Huang, L.; Linga, P. Effect of Wellbore Design on the Production Behaviour of Methane Hydrate-Bearing Sediments Induced by Depressurization. *Appl. Energy* **2019**, *254*, 113635. [\[CrossRef\]](#)
24. Li, L.; Li, X.; Wang, Y.; Qin, C.; Li, B.; Luo, Y.; Feng, J. Investigating the Interaction Effects between Reservoir Deformation and Hydrate Dissociation in Hydrate-Bearing Sediment by Depressurization Method. *Energies* **2021**, *14*, 548. [\[CrossRef\]](#)
25. Gao, Y.; Chen, Y.; Zhao, X.; Wang, Z.; Li, H.; Sun, B. Risk Analysis on the Blowout in Deepwater Drilling When Encountering Hydrate-Bearing Reservoir. *Ocean Eng.* **2018**, *170*, 1–5. [\[CrossRef\]](#)
26. Freij-Ayoub, R.; Tan, C.; Clennell, B.; Tohidi, B.; Yang, J. A Wellbore Stability Model for Hydrate Bearing Sediments. *J. Pet. Sci. Eng.* **2007**, *57*, 209–220. [\[CrossRef\]](#)
27. Khabibullin, T.; Falcone, G.; Teodoriu, C. Drilling through Gas Hydrate Sediments: Managing Wellbore Stability Risks. In Proceedings of the SPE EUROPEC/EAGE Annual Conference and Exhibition, Barcelona, Spain, 14–17 June 2010.
28. Ning, F.L.; Yu, Y.B.; Jiang, G.S.; Wu, X.; Zhang, K.N.; Zhang, L.; Liu, L. Numerical Simulations of Drilling Mud Invasion into the Marine Gas Hydrate-Bearing Sediments. *Adv. Mater. Res.* **2011**, *366*, 378–387. [\[CrossRef\]](#)
29. Ning, F.; Wu, N.; Yu, Y.; Zhang, K.; Jiang, G.; Zhang, L.; Sun, J.; Zheng, M. Invasion of Drilling Mud into Gas-Hydrate-Bearing Sediments. Part II: Effects of Geophysical Properties of Sediments. *Geophys. J. Int.* **2013**, *193*, 1385–1398. [\[CrossRef\]](#)
30. Sun, J.; Ning, F.; Lei, H.; Gai, X.; Sánchez, M.; Lu, J.; Li, Y.; Liu, L.; Liu, C.; Wu, N.; et al. Wellbore Stability Analysis during Drilling through Marine Gas Hydrate-Bearing Sediments in Shenhu Area: A Case Study. *J. Pet. Sci. Eng.* **2018**, *170*, 345–367. [\[CrossRef\]](#)
31. Yu, L.; Xu, Y.; Gong, Z.; Huang, F.; Zhang, L.; Ren, S. Experimental Study and Numerical Modeling of Methane Hydrate Dissociation and Gas Invasion during Drilling through Hydrate Bearing Formations. *J. Pet. Sci. Eng.* **2018**, *168*, 507–520. [\[CrossRef\]](#)
32. Gao, Y.; Chen, Y.; Wang, Z.; Chen, L.; Zhao, X.; Sun, B. Experimental Study on Heat Transfer in Hydrate-Bearing Reservoirs during Drilling Processes. *Ocean Eng.* **2019**, *183*, 262–269. [\[CrossRef\]](#)
33. Huang, T.; Li, X.; Zhang, Y.; Wang, Y.; Chen, Z. Experimental Study of the Drilling Process in Hydrate-Bearing Sediments under Different Circulation Rates of Drilling Fluid. *J. Pet. Sci. Eng.* **2020**, *189*, 107001. [\[CrossRef\]](#)
34. Wei, J.; Cheng, Y.; Yan, C.; Li, Q.; Zou, D.; Zhang, H. Drilling Parameter Optimizing Strategies to Prevent Hydrate Decomposition Risks. *Appl. Therm. Eng.* **2019**, *146*, 405–412. [\[CrossRef\]](#)
35. Huang, T.; Zhang, Y.; Li, G.; Li, X.; Chen, Z. Numerical Modeling for Drilling Fluid Invasion into Hydrate-Bearing Sediments and Effects of Permeability. *J. Nat. Gas Sci. Eng.* **2020**, *77*, 103239. [\[CrossRef\]](#)
36. Zhang, L.; Zhang, Y.; Chen, C.; Li, X.-S.; Chen, Z.-Y. Numerical Simulation of Hydrate Decomposition during the Drilling Process of the Hydrate Reservoir in the Northern South China Sea. *Energies* **2022**, *15*, 3273. [\[CrossRef\]](#)
37. Li, Q.; Liu, L.; Yu, B.; Guo, L.; Shi, S.; Miao, L. Borehole Enlargement Rate as a Measure of Borehole Instability in Hydrate Reservoir and Its Relationship with Drilling Mud Density. *J. Pet. Explor. Prod. Technol.* **2021**, *11*, 1185–1198. [\[CrossRef\]](#)
38. Zhao, X.; Zhao, Y.; Wang, Z.; Chen, G.; Li, P.; Liang, W.; Gao, X.; Xu, H.; Jiang, L.; Wei, N. Wellbore Temperature Distribution during Drilling of Natural Gas Hydrate Formation in South China Sea. *Petroleum* **2021**, *7*, 451–459. [\[CrossRef\]](#)
39. Li, X.; Sun, B.; Ma, B.; Li, H.; Liu, H.; Cai, D.; Wang, X.; Li, X. Study on the Evolution Law of Wellbore Stability Interface during Drilling of Offshore Gas Hydrate Reservoirs. *Energies* **2023**, *16*, 7585. [\[CrossRef\]](#)
40. Wang, Q.; Wang, R.; Sun, J.; Sun, J.; Lu, C.; Lv, K.; Wang, J.; Wang, J.; Yang, J.; Qu, Y. Effect of Drilling Fluid Invasion on Natural Gas Hydrate Near-Well Reservoirs Drilling in a Horizontal Well. *Energies* **2021**, *14*, 7075. [\[CrossRef\]](#)
41. Li, W.; Gao, D.; Yang, J. Study of Mud Weight Window of Horizontal Wells Drilled into Offshore Natural Gas Hydrate Sediments. *J. Nat. Gas Sci. Eng.* **2020**, *83*, 103575. [\[CrossRef\]](#)
42. Sun, J.; Ning, F.; Liu, T.; Li, Y.; Lei, H.; Zhang, L.; Cheng, W.; Wang, R.; Cao, X.; Jiang, G. Numerical Analysis of Horizontal Wellbore State during Drilling at the First Offshore Hydrate Production Test Site in Shenhu Area of the South China Sea. *Ocean Eng.* **2021**, *238*, 109614. [\[CrossRef\]](#)

43. Liao, Y.; Wang, Z.; Chao, M.; Sun, X.; Wang, J.; Zhou, B.; Sun, B. Coupled Wellbore–Reservoir Heat and Mass Transfer Model for Horizontal Drilling through Hydrate Reservoir and Application in Wellbore Stability Analysis. *J. Nat. Gas Sci. Eng.* **2021**, *95*, 104216. [\[CrossRef\]](#)
44. Sloan, E.D.; Koh, C.A. *Clathrate Hydrates of Natural Gases*, 3rd ed.; CRC Press: Boca Raton, FL, USA, 2008.
45. Masuda, Y. Numerical Calculation of Gas Production Performance from Reservoirs Containing Natural Gas Hydrates. In Proceedings of the SPE Asia Pacific Oil & Gas Conference & Exhibition, Kuala Lumpur, Malaysia, 14–16 April 1997.
46. Stone, H.L. Probability Model for Estimating Three-Phase Relative Permeability. *J. Pet. Technol.* **1970**, *22*, 214–218. [\[CrossRef\]](#)
47. Van Genuchten, M.T. A Closed-Form Equation for Predicting the Hydraulic Conductivity of Unsaturated Soils. *Soil Sci. Soc. Am. J.* **1980**, *44*, 892–898. [\[CrossRef\]](#)
48. Kim, H.C.; Bishnoi, P.R.; Heidemann, R.A.; Rizvi, S.S.H. Kinetics of Methane Hydrate Decomposition. *Chem. Eng. Sci.* **1987**, *42*, 1645–1653. [\[CrossRef\]](#)
49. Moridis, G.J. Numerical Studies of Gas Production from Methane Hydrates. *Soc. Pet. Eng.* **2002**, *8*, 359–370.
50. Clarke, M.; Bishnoi, P.R. Determination of the Activation Energy and Intrinsic Rate Constant of Methane Gas Hydrate Decomposition. *Can. J. Chem. Eng.* **2001**, *79*, 143–147. [\[CrossRef\]](#)
51. Malegaonkar, M.B.; Dholabhai, P.D.; Bishnoi, P.R. Kinetics of Carbon Dioxide and Methane Hydrate Formation. *Can. J. Chem. Eng.* **2009**, *75*, 1090–1099. [\[CrossRef\]](#)
52. Englezos, P.; Kalogerakis, N.; Dholabhai, P.D.; Bishnoi, P.R. Kinetics of Formation of Methane and Ethane Gas Hydrates. *Chem. Eng. Sci.* **1987**, *42*, 2647–2658. [\[CrossRef\]](#)
53. Sun, X.; Mohanty, K.K. Kinetic Simulation of Methane Hydrate Formation and Dissociation in Porous Media. *Chem. Eng. Sci.* **2006**, *61*, 3476–3495. [\[CrossRef\]](#)
54. Wang, H.; Li, Y.; Huang, L.; Liu, T.; Liu, W.; Wu, P.; Song, Y. A Pore-Scale Study on Microstructure and Permeability Evolution of Hydrate-Bearing Sediment during Dissociation by Depressurization. *Fuel* **2024**, *358*, 130124. [\[CrossRef\]](#)
55. Hillman, J.I.T.; Burwicz, E.; Zander, T.; Bialas, J.; Klaucke, I.; Feldman, H.; Drexler, T.; Awwiller, D. Investigating a Gas Hydrate System in Apparent Disequilibrium in the Danube Fan, Black Sea. *Earth Planet. Sci. Lett.* **2018**, *502*, 1–11. [\[CrossRef\]](#)
56. Burton, Z.F.M.; Dafov, L.N. Testing the Sediment Organic Contents Required for Biogenic Gas Hydrate Formation: Insights from Synthetic 3-D Basin and Hydrocarbon System Modelling. *Fuels* **2022**, *3*, 555–562. [\[CrossRef\]](#)
57. Kroeger, K.F.; Crutchley, G.J.; Hillman, J.I.T.; Turco, F.; Barnes, P.M. Gas Hydrate Formation Beneath Thrust Ridges: A Test of Concepts Using 3D Modelling at the Southern Hikurangi Margin, New Zealand. *Mar. Pet. Geol.* **2022**, *135*, 105394. [\[CrossRef\]](#)
58. Burton, Z.F.M.; Kroeger, K.F.; Hosford Scheirer, A.; Seol, Y.; Burgreen-Chan, B.; Graham, S.A. Tectonic Uplift Destabilizes Subsea Gas Hydrate: A Model Example from Hikurangi Margin, New Zealand. *Geophys. Res. Lett.* **2020**, *47*, e2020GL087150. [\[CrossRef\]](#)
59. Burwicz, E.; Reichel, T.; Wallmann, K.; Rottke, W.; Haeckel, M.; Hensen, C. 3-D Basin-Scale Reconstruction of Natural Gas Hydrate System of the Green Canyon, Gulf of Mexico. *Geochem. Geophys. Geosyst.* **2017**, *18*, 1959–1985. [\[CrossRef\]](#)
60. Burton, Z.F.M.; Dafov, L.N. Salt Diapir-Driven Recycling of Gas Hydrate. *Geochem. Geophys. Geosyst.* **2023**, *24*, e2022GC010704. [\[CrossRef\]](#)

**Disclaimer/Publisher’s Note:** The statements, opinions and data contained in all publications are solely those of the individual author(s) and contributor(s) and not of MDPI and/or the editor(s). MDPI and/or the editor(s) disclaim responsibility for any injury to people or property resulting from any ideas, methods, instructions or products referred to in the content.